The Viscoelastic Poisson's ratio of Webs

By

CLEMENT BROUSSE

Bachelor of Science (B.Sc.) in Mechanical Engineering
Ecole Catholique des Arts et Métiers
67300 Schiltigheim, FRANCE
2017

Master of Engineering (M.Eng.) in Mechanical Engineering
Ecole Catholique des Arts et Métiers
67300 Schiltigheim, FRANCE
2017

Submitted to the Faculty of the
Graduate College of the
Oklahoma State University
in partial fulfillment of
the requirements for
the Degree of
Master of Science
December 2020

The Viscoelastic

Poisson's ratio

of Webs

Dissertation Approved:

Dr. Aurelie Azoug

Dissertation Advisor

Dr. James Manimala

Dr. James Keith Good

ACKNOWLEDGMENTS

First of all, I would like to thanks my advisor Dr. Azoug for her advice, who led me to the results presented here. This research work would not have been possible without her guidance. She granted me a comfortable freedom and often challenged my views to grow my knowledge.

Furthermore, I want to thank to my committee members Dr. Good and Dr. Manimala for their suggestions and help to perform this work. I would additionally thank Dr. Manimala who welcomed me in his laboratory and patiently advised me to pursue my project.

I thank the Web Handling Research Center, including all its sponsors, for their financial support to this study, as well as Kimberly-Clark Corporation (Neenah, WI) for providing the non-woven used for my research.

I thank my colleagues and friends for the challenging discussions we had as well as their support during and after working hours last years.

Finally, I am deeply indebted to my parents Catherine Leclaircie and Bernard Brousse as well as my relatives for their unconditional trust and support. I am lucky to have them on my side – always encouraging me to pursue my dreams even though we are physically apart.

Acknowledgments reflect the views of the author and are not endorsed by committee members or Oklahoma State University.

Name: CLEMENT BROUSSE

Date of Degree: DECEMBER 2020

Title of Study: THE VISCOELASTIC POISSON'S RATIO OF WEBS

Major Field: MECHANICAL AND AEROSPACE ENGINEERING

Abstract: During web handling operations, the web moves along a processing line, supported by rollers, and is subject to numerous successive processes, for example several printing operations with different colors. Registration errors are caused by a change in web position between two different prints. The displacement between the different prints blurs the printed pattern. Often, products with registration errors are rejected by the customers so industrials try to reduce them as much as possible. Predicting the exact lateral position of the web during the web handling process remains difficult due to the time-dependent behavior of the web. The material property controlling this process parameter is the Viscoelastic Poisson's Ratio (VPR).

The theory of the VPR is presented and the VPRs of different webs, low-density polyethylene (LDPE oriented and non-oriented) and nonwoven (polypropylene), are measured using Digital Image Correlation during stress relaxation and creep. The heterogeneity of the full field strains and its temporal variations are discussed. The influences on the VPR of the test, the material, its orientation, and the size of the specimen are studied with multiple ANOVAs. Finally, we present the error engendered by considering the Poisson's ratio constant instead of considering the VPR in a time-dependent model and the consequences on the registration error during an industrial process.

The orientation is a factor influencing the VPR for anisotropic materials. Moreover, the influence of the size depends of the homogeneity of the material. For heterogenous materials, the specimen size influences the long relaxation time of the VPR. Furthermore, the strain fields recorded for the LDPEO and NW present strong heterogeneities. These heterogeneities can increase the registration errors if they occur at a printing location. Finally, the position error engendered by considering the elastic Poisson's ratio instead of the VPR can reach a few millimeters, leading to noticeable registration erros. In conclusion, the VPR is particularly important for heterogeneous materials such as non-woven webs.

TABLE OF CONTENTS

LIST OF TABLES

LIST OF FIGURES

CHAPTER I

BACKGROUND

1.1 Web handling and viscoelasticity

1.1.1 Definition of a web

A web is defined as a continuous structure which exhibits a much larger length than its thickness and width. In other words, webs are long, thin, flexible strips of materials. Webs are made of materials such as paper, polymers, and woven or nonwoven fabrics. Webs are commonly used in everyday life as food packaging, plastic bags, hygienic products, but also in more complex applications, such as electronics and high-technology optics.

Figure 1: Example of a roll of paper web [Dogumak, 2020]

The most practical way to store and move a web is in the form of a roll (Fig. 1),

where the web is wound around a rigid core that allows for transportation as well as unwinding.

One common difficulty of processing webs is the potential anisotropy of the material considered. The material anisotropy results from the manufacturing process. While some webs can safely be considered as close to isotropic, some are anisotropic, most often orthotropic. For an orthotropic web, the orientation is defined by two orthogonal directions (Fig. 2). The principal direction of the web is called *machine direction* (MD) while the orthogonal direction is the *cross-machine direction* (CMD). Properties in the third direction are identical to the properties in the CMD.

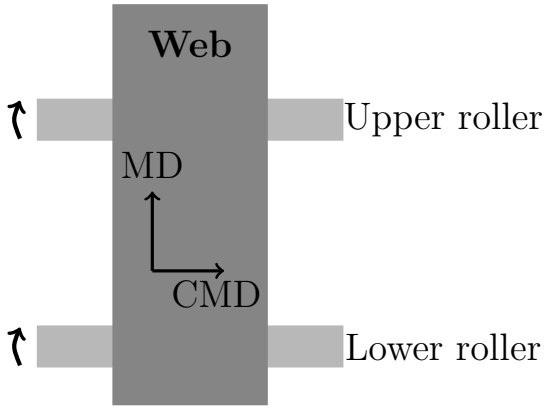

Figure 2: Definition of MD and CMD on a web span.

1.1.2 Web handling

The webs are processed in continuous manufacturing processes, often called roll-to-roll (R2R) processes. While a continuous process allows high-speed automated manufacturing operations, it also imposes more challenges than discontinuous processes. In a continuous process, the system should be able to dynamically regulate itself and the web dynamics to avoid damaging the web. Achieving proper regulation will result in shorter processing times, increase in the final product quality, and reduction in throwaway material. Web handling is the discipline of science and technology aim-

ing at achieving highly-functioning processes of webs, by studying the out-of-plane deformations, the webs dynamics, and the webs properties.

The typical R2R process is composed of an unwind station, where a shaft is used to unroll the web, a series of intermediate processing stations, and a winding station, where the web is wound back in a roll. As the web moves over rollers, its lateral position and longitudinal tension can become unstable. These instabilities cause web handling issues and reduce the quality of the final product [Shi, 2019].

There are multiple strategies and adjustments applied by web handling engineers to reduce the amount of errors in the process. One strategy to accurately move the web along the process is to correctly align the rollers using a small enough tolerance. In addition, the rollers should be balanced to avoid additional vibrations. An ideal friction between the rollers and the web improves the transmission of torque between rollers and web and avoids web slippage [Roisum, 1995].

The two most common out-of-plane instabilities are troughs and wrinkles. A trough appears in the free span of the web between rollers while a wrinkle appears during the motion of the web over a roller. The troughs do not necessarily impact the quality of the final product but the wrinkles always do [Good et al., 1997]. Both troughs and wrinkles originate from a stress along the CMD.

1.1.3 Registration errors

To print a defined pattern on the web, the web passes through a series of printing units, one for each color of the multicolored pattern. The printing process consists in overlapping each color to form the final image. A registration error bigger than 0.01 mm (0.004 in) is perceptible to the human eye [Paukku & Parola, 2004] and will affect the perceived quality of the printed image. One common example is the color printing process on a web like paper. During this process, each color should correctly overlap to avoid a blurry image. Nowadays, the R2R process is also used

for printing electronic components on a flexible surface [Noh et al., 2010], such as capacitor, electrode, or connecting wires. This requires high spatial accuracy, on the order of a few μm. An error while printing a wire would undermine the functionality of the entire circuit.

The misalignment of the web arriving to a roll is a direct cause of registration error [Shi, 2019, Lee et al., 2020]. The control of the spatial position of the web throughout the process is essential.

Changes in the spatial position of the web also result from variations in web tension. These variations can cause the web to wrinkle, crease, or even break [Seshadri et al., 2013]. The variation in tension on the substrate also influences the roughness of the substrate, which changes the contact angle of the ink. The influence of the tension on the ink rheological properties is an additional cause of the registration error [Park et al., 2018].

Several measures can control the tension variation in line [Lee et al., 2020]. The web tension can be controlled through the speed of the web, which, in turn, can be regulated by the speed of the rollers [Seshadri & Pagilla, 2013]. One measure consists in measuring the tension with a load cell and regulating it through a PID controller. Another option is to include an accumulator, which is a series of rolls modifying the web speed, hence regulating the tension. The last option is to use a dancer, *i.e.* a mechanical component linked on one side to a roll and on the other side to a viscoelastic system [Dwivedula et al., 2006]. Dancers are designed to damp fluctuations. The active dancer moves laterally while the passive dancer rotates. Although active dancers are more accurate than the passive ones, most dancers do not efficiently damp sudden forces [Lee et al., 2020].

Whether the spatial misalignment is due to web tension or to other factors, it needs to be controlled and predicted in order to avoid registration errors. In order to do so, several models and methods have been developed [Seshadri et al., 2013, Li

et al., 2020]. These models rely heavily on the ability to characterize the mechanical properties of the webs, including their time-dependent properties.

1.1.4 Importance of viscoelasticity in web handling

Time influences R2R processes in multiple ways. During the R2R process, webs are subject to constant tension. This tension leads to creep, that is changes in length, which in turn can result in defects such as bagging.

As has been alluded to in the previous section, predictions of the web behavior during the R2R process highly depends on the researcher's ability to include the time-dependence of the material properties in the models. For example, the registration models all assume a constant (elastic) Poisson's ratio to determine the relationships between MD tension and CMD displacements. This assumption, although common and often valid, may lead to errors in the prediction of the lateral position of the web on the line.

In addition, webs exhibit viscoelastic curl at unwinding as a direct result of viscoelastic creep [Pan et al., 2020]. Experiments on Low-Density PolyEthylene (LDPE) have shown that, when the web is stored in a wound roll for extended periods, it will exhibit a curvature at unwinding. This curl originates from imposed stresses at winding leading to viscoelastic creep. Because this curl is viscoelastic, it is also reversible. However, the time needed for the web to relax and regain its flat configuration is prohibitive compared to common processing times.

In addition to these remarks focused on the general processes of unwinding, moving through the line, and rewinding webs, the actual manufacturing processes performed on the line are also influenced by the viscoelasticity of the material [Deng et al., 2015].

1.2 The viscoelastic Poisson's ratio (VPR)

The well-known Poisson's effect is defined as the lateral contraction of a material uniaxially stretched in the longitudinal direction. The Poisson's ratio (PR) is the negative ratio of lateral strain and longitudinal strain. The PR is generally assumed constant for all materials. However, this assumption is rarely verified for viscoelastic materials whose properties are all time-dependent. A complete theoretical definition of PR and VPR is given in Chapter II. This section is focused on a literature survey of the VPR, its measurement and implications.

1.2.1 VPR in isotropic materials

Homogeneous materials

A direct measurement of the VPR was performed at room temperature (23.6°C) for low density polyethylene [Delin et al., 1995]. The strain rate used is 3.03 %/min until the maximal strain of 0.22 - 0.33 % is reached. The lateral strain does not show any local extremum and evolves linearly with respect to the longitudinal strain, suggesting the tests are performed within the limits of linear viscoelastic behavior. The VPR shows the expected increase according to time. The VPR measurements at different longitudinal strains show an increase in VPR with strain.

The response of a beamlike specimen to a prescribed strain wave has been recorded using strain gauges at room temperature [Giovagnoni, 1994]. Specimens are made of different polymers, such as PVCs, Plexiglas, polyamide, polyacetalic, and PTFE. The resulting VPR is relatively frequency-independent over the tested range. This minimal variation of the VPR with frequency has been attributed to the fact that the materials were in the glassy region [Tschoegl et al., 2002].

Similarly, the frequency-dependent VPR of poly(methyl-methacrylate) (PMMA) has been measured imposing a wave with a 0.1% peak-to-peak strain superimposed on

a 0.02 to 0.06 % minimum tensile strain [Yee & Takemori, 1982]. The VPR is reported at three temperatures, 0°C, 20°C, 40°C, at frequencies between 0.01 Hz and 10 Hz. The absolute value of the frequency-dependent VPR shows a monotone decrease with an increasing frequency, except at 0°C, where the VPR reaches an extremum around 0.4 Hz.

The VPR of poly(methyl-methacrylate) has been measured with the Moiré method [Lu et al., 1997]. The master curve presented shows a monotone increasing behavior. Because measuring the very small lateral strains is challenging, the obtained master curve of the VPR at 110°C is not smooth. For a longitudinal strain of 0.2%, the transverse strains are between 0.06% and 0.1%.

The study of polycarbonate under stress relaxation at room temperature shows an almost constant VPR as a function of time during 4 decades [Tsou et al., 1995]. The constant VPR can be explained by the temperature. The glass transition temperature of the polycarbonate is close to 148°C [Wang et al., 2016, Negahban et al., 2007]. As these experiments are done far below the glass transition, the time-dependence of the material behavior is not important enough to be measured [Tschoegl et al., 2002].

The strains in a dumbbell specimen of cold setting epoxy polymer, C-100-0-8, are measured with a Tuckerman gauge in order to indirectly evaluate the VPR [Theocaris, 1964]. The convolution integral solution is approximated by knowing the bulk creep compliance and relaxation modulus. The VPR computed from the creep compliance differs from the one computed from the relaxation modulus. This difference has been attributed to the approximation in the estimation of the integral [Tschoegl et al., 2002].

Heterogeneous materials

Lateral and longitudinal strains in a Hypalon-based rubber with varying glass-bead-filler concentration have been measured using optical methods [Kugler et al., 1990].

A coherent light is reflected on a series of parallel contrasting strips on the specimen. The distance between the strips is obtained by measuring the time required for the light to reach the light sensor. The VPR increases with time without reaching any plateau or equilibrium for different level of strains. Similarly to homogeneous polymers, an increase in VPR with strain is observed.

The asphalt VPR strictly increases with time during a stress relaxation test, a compression test, and a strain to failure test [Kassem et al., 2013]. The VPR increases in unconfined tension and compression and decreases in confined compression. This is attributed to a difference in the rate of increase or decrease of the shear compliance and dilatation compliance. The increase of the VPR is attributed to a faster evolution of the shear compliance than the dilatation compliance [Alanazi et al., 2019]. The VPR is also pressure-dependent. VPR measurements on asphalt from tension and compression tests [Alanazi et al., 2019] show a strong influence of the structure, that is the size of the aggregates. Coarser aggregates lead to a lower VPR. Moisture also influences the VPR, probably because of a variation of the adhesion between the asphalt binder and the aggregates allowing a larger deformation in the transverse direction. Aging, accelerated by imposing a high temperature during few hours, is believed to influence the air void content and modify the VPR of the aged material [Mehrez et al., 2015].

The VPRs of a polypropylene homopolymer, a glass bead-filled polypropylene, and talc-filled polypropylene are measured by Digital Image Correlation (DIC) and compared [Tscharnuter et al., 2011b]. The VPR of both the polypropylene and glass bead-filled polypropylene increase monotonically from 10 to 10^4 s during a relaxation test. A VPR master curve at 23°C is also computed from creep tests. The VPR increases with time from 0.42 to 0.45. The data is scattered below 10s.

1.2.2 VPR in anisotropic materials

The VPR of transversely isotropic films of cellulose acetate is measured by a stress relaxation test between 10 s and 10^5 s at room temperature [Tsou et al., 1995]. The VPR presents a parabolic curve with an extrema at 10^2 s, which differs from other literature values where the VPR is a monotonic function of the time. The authors attributed this peak to a heterogeneity of the solvent and moisture in the film. The solvent may redistribute itself in the specimen during the test leading to a heterogeneous strain distribution. However, this result has also been reported as experimental error because the tests were performed below the glass transition temperature of the material [Tschoegl et al., 2002]. The glass transition temperature of the cellulose acetate is between $166°C$ and $206°C$ [Kamide & Saito, 1985]. As the material was tested in the glassy region, a constant VPR was expected.

A multiscale model of a highly-anisotropic composite made of 3D interlock woven reinforcement and an epoxy matrix is performed through two consecutive homogenization steps [Hirsekorn et al., 2018]. The first homogenization estimates the viscoelastic behavior of the warp and weft yarns at the microscopic scale. The second homogenization is done at the macroscopic scale on the matrix behavior. The resulting homogenized viscoelastic model represents the global behavior of the composite. The VPR simulated during stress relaxation shows a plateau up to 60 s and an increase from 60 s to 10^4s from 0.4 to 0.9 [Hirsekorn et al., 2018].

1.2.3 Research objectives

Some web defects are due to a faulty prediction of the exact lateral position of the web on the roll-to-roll line. Models often assume a time-independent Poisson's ratio as the web material constant. Measurements and studies of the time-dependent Poisson's ratio can be found in the literature, but very few focus on webs and fewer on the factors influencing this VPR.

The goal of this work is to investigate the influence of the VPR on the estimation of the lateral position of the web. The main long-term objective is to determine if the VPR is relevant to future models of the webs mechanical behavior. This study will also compare and systematically determine the influence of the material, its orientation for anisotropic webs, and specimen size, on the value and time evolution of the VPR.

CHAPTER II

THEORETICAL ASPECTS

2.1 Definition of the elastic Poisson's ratio

2.1.1 Isotropic materials

The Poisson's ratio (PR) ν of isotropic materials is usually defined for an infinitesimal elastic deformation as the negative ratio of the transverse strains over the axial strains in a uniaxial test [Poisson, 1829]. The orientation of the specimen is given by Figure 3.

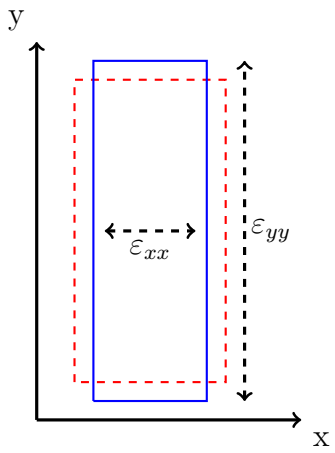

Figure 3: Schematic of the Poisson's effect. The rectangular specimen is dashed before deformation and in full line after deformation. The specimen is assumed to be stretched along the y axis.

For a specimen stretched along the y axis, the PR is defined as:

$$\nu = -\frac{\varepsilon_{xx}}{\varepsilon_{yy}} \tag{2.1.1}$$

where ε_{xx} is the strain along the x axis and ε_{yy} is the strain along the y axis. The definition (2.1.1) assumes the mechanical properties do not exhibit any time-dependence. While this assumption is not physically realistic for viscoelastic materials, it is a valuable assumption for materials where the time-dependence may be small enough to be neglected, such as metals, woods, or some plastics.

The PR can also be expressed as a function of the bulk modulus K and the shear modulus G as [Tschoegl, 1989]

$$\nu = \frac{3K - 2G}{6K + 2G}. \tag{2.1.2}$$

For an isotropic elastic material, the Young's modulus E is positive and can be classically expressed as a function of K and G with $E = 9KG/(3K + G)$. Hence, E is positive if K and G are positive, leading to limits on ν.

$$0 \leq K \quad \rightarrow \quad -1 \leq \nu \tag{2.1.3}$$

$$0 \leq G \quad \rightarrow \quad \nu \leq \frac{1}{2} \tag{2.1.4}$$

As a result, for an isotropic elastic material, $-1 \leq \nu \leq \frac{1}{2}$. Most materials have a PR between 0 and 1/2. A perfectly incompressible material has a PR of exactly 1/2.

Interestingly, this also implies that the PR can be negative. Materials who exhibit this specific and unusual behavior are called auxetic. Under stretching in the longitudinal direction, the material expands in the lateral direction. Auxetic materials can be used for wave damping or for shoes able to slightly grow if the feet inflates. This behavior can be intrinsic to the material or introduced by creating a specific structure at a small scale, typically with metamaterials [Dobnik Dubrovski et al., 2019]. As an example, a needle-punched non-woven fabric can be cut with a laser to form rotating unit cells, where the squared unit cells are linked at one extremity (Figs. 4a and 4b).

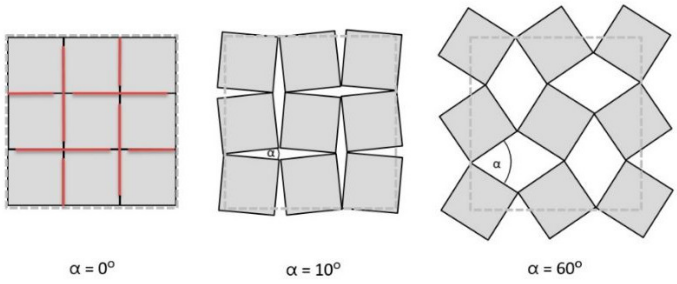

(a) Cell before loading (left) and after loading (center and right) [Dobnik Dubrovski et al., 2019].

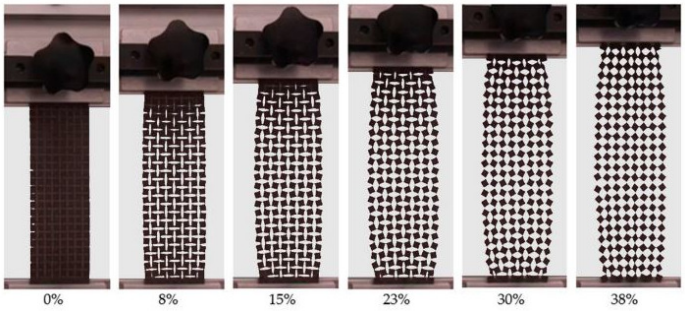

(b) Tensile test of an auxetic specimen [Dobnik Dubrovski et al., 2019].

Figure 4: Auxetic behavior of a needle-punched non-woven fabric. The auxetic behavior is created by the geometry of the cells.

2.1.2 Anisotropic materials

For an anisotropic material, the PR can have higher values than 0.5. For example, the PR of a fiber-reinforced plastic has been measured close to 0.8 [Kimoto et al., 1990]. The PR of an anisotropic material depends on the direction of the uniaxial stretching, which defines the longitudinal axis and the lateral direction considered,

$$\nu_{xy} = -\frac{\varepsilon_{xx}}{\varepsilon_{yy}} \text{ and } \nu_{yx} = -\frac{\varepsilon_{yy}}{\varepsilon_{xx}} \tag{2.1.5}$$

and,

$$\nu_{xy} \neq \nu_{yx}. \tag{2.1.6}$$

Fully characterizing an anisotropic material requires a large number of elastic constants. If the material exhibits any plane of symmetry, the number of elastic constants required is reduced. For example, characterizing orthotropic materials (3 mutually orthogonal symmetry planes) requires 9 different constants: 3 shear moduli, 3 stress moduli, and 3 PRs.

2.2 Poisson's ratio in orthotropic materials

An orthotropic material is defined as a medium with three-orthogonal symmetry plans. Most anisotropic webs are considered orthotropic.

2.2.1 Symmetry of the stiffness matrix

To simplify the notation of the stiffness matrix, the following notation is used for the indices:

$$\begin{bmatrix} 1 \\ 2 \\ 3 \\ 4 \\ 5 \\ 6 \end{bmatrix} \longrightarrow \begin{bmatrix} xx \\ yy \\ zz \\ yz \\ xz \\ xy \end{bmatrix}$$

Hence $\mathbb{C}_{xxyy}$ can be written as $\mathbb{C}_{12}$.

All the following tensorial calculations are carried out in an orthonormal basis corresponding to the symmetry planes of the materials. The stiffness matrix $\mathbb{C}$ in Hooke's law relates the stress σ to the strain ε tensors.

$$\sigma = \mathbb{C}\varepsilon \tag{2.2.1}$$

As the material properties exhibits symmetries, the stiffness matrix is invariant under orthogonal transformations along the material's symmetry. For example, the

reflexion with respect to a plane with the x axis as a normal is

$$L = \begin{bmatrix} -1 & 0 & 0 \\ 0 & 1 & 0 \\ 0 & 0 & 1 \end{bmatrix} \tag{2.2.2}$$

The stiffness matrix is invariant under an orthogonal transformation L if and only if

$$\mathbb{C} = \mathbf{L}^T\mathbf{L}^T\mathbb{C}\mathbf{L}\mathbf{L}. \tag{2.2.3}$$

which leads to

$$\begin{bmatrix} \mathbb{C}_{11} & \mathbb{C}_{12} & \mathbb{C}_{13} & \mathbb{C}_{14} & \mathbb{C}_{15} & \mathbb{C}_{16} \\ \mathbb{C}_{12} & \mathbb{C}_{22} & \mathbb{C}_{23} & \mathbb{C}_{24} & \mathbb{C}_{25} & \mathbb{C}_{26} \\ \mathbb{C}_{13} & \mathbb{C}_{23} & \mathbb{C}_{33} & \mathbb{C}_{34} & \mathbb{C}_{35} & \mathbb{C}_{36} \\ \mathbb{C}_{14} & \mathbb{C}_{24} & \mathbb{C}_{34} & \mathbb{C}_{44} & \mathbb{C}_{45} & \mathbb{C}_{46} \\ \mathbb{C}_{15} & \mathbb{C}_{25} & \mathbb{C}_{35} & \mathbb{C}_{45} & \mathbb{C}_{55} & \mathbb{C}_{56} \\ \mathbb{C}_{16} & \mathbb{C}_{26} & \mathbb{C}_{36} & \mathbb{C}_{46} & \mathbb{C}_{56} & \mathbb{C}_{66} \end{bmatrix} = \begin{bmatrix} \mathbb{C}_{11} & \mathbb{C}_{12} & \mathbb{C}_{13} & \mathbb{C}_{14} & -\mathbb{C}_{15} & -\mathbb{C}_{16} \\ \mathbb{C}_{12} & \mathbb{C}_{22} & \mathbb{C}_{23} & \mathbb{C}_{24} & -\mathbb{C}_{25} & -\mathbb{C}_{26} \\ \mathbb{C}_{13} & \mathbb{C}_{23} & \mathbb{C}_{33} & \mathbb{C}_{34} & -\mathbb{C}_{35} & -\mathbb{C}_{36} \\ \mathbb{C}_{14} & \mathbb{C}_{24} & \mathbb{C}_{34} & \mathbb{C}_{44} & -\mathbb{C}_{45} & -\mathbb{C}_{46} \\ -\mathbb{C}_{15} & -\mathbb{C}_{25} & -\mathbb{C}_{35} & -\mathbb{C}_{45} & \mathbb{C}_{55} & \mathbb{C}_{56} \\ -\mathbb{C}_{16} & -\mathbb{C}_{26} & -\mathbb{C}_{36} & -\mathbb{C}_{46} & \mathbb{C}_{56} & \mathbb{C}_{66} \end{bmatrix} \tag{2.2.4}$$

The equation (2.2.4) is valid if and only if $\mathbb{C}_{15}, \mathbb{C}_{16}, \mathbb{C}_{25}, \mathbb{C}_{26}, \mathbb{C}_{35}, \mathbb{C}_{36}, \mathbb{C}_{45}, \mathbb{C}_{46}$ are all equal to zero.

The stiffness matrix with a reflection along the x axis is then

$$\mathbb{C}_1 = \begin{bmatrix} \mathbb{C}_{11} & \mathbb{C}_{12} & \mathbb{C}_{13} & \mathbb{C}_{14} & 0 & 0 \\ \mathbb{C}_{12} & \mathbb{C}_{22} & \mathbb{C}_{23} & \mathbb{C}_{24} & 0 & 0 \\ \mathbb{C}_{13} & \mathbb{C}_{23} & \mathbb{C}_{33} & \mathbb{C}_{34} & 0 & 0 \\ \mathbb{C}_{14} & \mathbb{C}_{24} & \mathbb{C}_{34} & \mathbb{C}_{44} & 0 & 0 \\ 0 & 0 & 0 & 0 & \mathbb{C}_{55} & \mathbb{C}_{56} \\ 0 & 0 & 0 & 0 & \mathbb{C}_{56} & \mathbb{C}_{66} \end{bmatrix} \tag{2.2.5}$$

Similarly, when the plane of symmetry is orthogonal to the y or z axis, the transfor-

mation matrix is

$$L = \begin{bmatrix} 1 & 0 & 0 \\ 0 & -1 & 0 \\ 0 & 0 & 1 \end{bmatrix} \qquad \text{or} \qquad L = \begin{bmatrix} 1 & 0 & 0 \\ 0 & 1 & 0 \\ 0 & 0 & -1 \end{bmatrix}. \tag{2.2.6}$$

By combining the 3 symmetries, the stiffness matrix for the orthotropic material is

$$\mathbb{C}_{ortho} = \begin{bmatrix} \mathbb{C}_{11} & \mathbb{C}_{12} & \mathbb{C}_{13} & 0 & 0 & 0 \\ \mathbb{C}_{12} & \mathbb{C}_{22} & \mathbb{C}_{23} & 0 & 0 & 0 \\ \mathbb{C}_{13} & \mathbb{C}_{23} & \mathbb{C}_{33} & 0 & 0 & 0 \\ 0 & 0 & 0 & \mathbb{C}_{44} & 0 & 0 \\ 0 & 0 & 0 & 0 & \mathbb{C}_{55} & 0 \\ 0 & 0 & 0 & 0 & 0 & \mathbb{C}_{66} \end{bmatrix}. \tag{2.2.7}$$

2.2.2 Resulting compliance tensor

The elastic compliance is the inverse of the elastic stiffness tensor. And this compliance can be expressed as a function of the moduli and PRs in the different directions.

$$\mathbb{S}_{ortho} = \begin{bmatrix} \mathbb{S}_{11} & \mathbb{S}_{12} & \mathbb{S}_{13} & 0 & 0 & 0 \\ \mathbb{S}_{12} & \mathbb{S}_{22} & \mathbb{S}_{23} & 0 & 0 & 0 \\ \mathbb{S}_{13} & \mathbb{S}_{23} & \mathbb{S}_{33} & 0 & 0 & 0 \\ 0 & 0 & 0 & \mathbb{S}_{44} & 0 & 0 \\ 0 & 0 & 0 & 0 & \mathbb{S}_{55} & 0 \\ 0 & 0 & 0 & 0 & 0 & \mathbb{S}_{66} \end{bmatrix} = \begin{bmatrix} \frac{1}{E_1} & -\frac{\nu_{21}}{E_2} & -\frac{\nu_{31}}{E_3} & 0 & 0 & 0 \\ -\frac{\nu_{12}}{E_1} & \frac{1}{E_2} & -\frac{\nu_{32}}{E_3} & 0 & 0 & 0 \\ -\frac{\nu_{13}}{E_1} & -\frac{\nu_{23}}{E_2} & \frac{1}{E_3} & 0 & 0 & 0 \\ 0 & 0 & 0 & -\frac{1}{G_{23}} & 0 & 0 \\ 0 & 0 & 0 & 0 & -\frac{1}{G_{31}} & 0 \\ 0 & 0 & 0 & 0 & 0 & -\frac{1}{G_{12}} \end{bmatrix} \tag{2.2.8}$$

For an orthotropic material, $\mathbb{S}_{ij} = \mathbb{S}_{ji}$. This gives the relation between the PRs in different directions $\frac{\nu_{ji}}{E_i} = \frac{\nu_{ij}}{E_j}$.

2.3 Viscoelastic Poisson's ratio VPR

The VPR cannot be directly defined by the negative ratio of the time-dependent strains along each orthogonal direction. This would imply the VPR as a material property depends on the longitudinal strain history of the specimen. As a result, the VPR values of two specimens from the same material would not be identical. The analytical expression used to compute the VPR depends on the strain and stress applied to the specimen. The following section details the theory behind determining the actual VPR from experimental data.

2.3.1 Measurements through stress relaxation tests

The VPR is defined as the lateral contraction ratio measured in response to a longitudinal step strain [Tschoegl et al., 2002], that is under the conditions of a stress relaxation test. In a stress relaxation test, the longitudinal strain is:

$$\varepsilon_{yy}(t) = \varepsilon_0 h(t) \tag{2.3.1}$$

where ε_0 is a constant and $h(t)$ is the Heaviside function defined as

$$h(t) = \begin{cases} 1, & \text{if } t \geq 0 \\ 0, & \text{otherwise} \end{cases} \tag{2.3.2}$$

and the ratio of the strains is

$$\nu(t) = -\frac{\varepsilon_{xx}(t)}{\varepsilon_{yy}(t)} \tag{2.3.3}$$

From (2.3.1) and (2.3.3), the expression of the VPR for any $t \geq 0$ is

$$\nu(t) = -\frac{\varepsilon_{xx}(t)}{\varepsilon_0} \tag{2.3.4}$$

By selecting the origin of the time at the beginning of the test, the relation (2.3.4) is valid during any stress relaxation test.

2.3.2 Generalization to any strain history

Equation (2.3.4) limits the analysis to a given strain history. To generalize this equation to any strain history, the equation should be transformed by using the correspondence principle with the Laplace transform [Kreyszig, 2012].

The **correspondence principle** is defined by "if an elastic solution to a boundary value problem (stress analysis problem) is known, substitution of the appropriate Laplace transforms for the quantities employed in the elastic analysis furnishes the viscoelastic solution in the transform plane. The time-dependent viscoelastic solution is then obtained by inverting the transform." [Tschoegl, 1989].

The Laplace transform of a function $f(t)$, with s the Laplace variable, is defined as

$$\mathcal{L}\left[f(t)\right] = \bar{f}(s) = \int_0^\infty f(t)e^{-st}dt \tag{2.3.5}$$

To define the VPR for any strain history, we apply the Laplace transform to equation (2.3.3), leading to

$$-\bar{\varepsilon}_{xx}(s) = \bar{\nu}_{exp}(s)\bar{\varepsilon}_{yy}(s) \tag{2.3.6}$$

where $\bar{\varepsilon}_{yy}(s)$ is the Laplace transform of $\varepsilon_{yy}(t)$, $\bar{\varepsilon}_{xx}(s)$ the Laplace transform of $\varepsilon_{xx}(t)$, and $\bar{\nu}_{exp}(s)$ the Laplace transform of the measured VPR as the ratio of the strains.

The expression is simplified by introducing the Carson transform $\mu(s)$ (also called s-Laplace transform) of $\nu(s)$ such as $\nu(s) = s\mu(s)$.

$$-\bar{\varepsilon}_{xx}(s) = s\bar{\mu}_{exp}(s)\varepsilon_{yy}(s) \tag{2.3.7}$$

where μ_{exp} designates the negative ratio of the measured strains. For a stress relaxation test, μ_{exp} is identical to the VPR.

2.3.3 Measurement through creep tests

For a creep test, the longitudinal strain is the product of the stress and the creep compliance $D(t)$.

$$\varepsilon_{yy}(s) = \bar{D}(s)\sigma_0. \tag{2.3.8}$$

where σ_0 is the constant stress of the creep test and $\bar{D}(s)$ is the Laplace transform of the creep compliance $D(t)$.

The longitudinal strain ε_0 is defined as the amplitude of the longitudinal strain step necessary to generate the same transverse strain as the one measured during the creep test. Equation (2.3.7) is rearranged as

$$\bar{\nu}(s)\varepsilon_0 = s\bar{\mu}_{creep}(s)\bar{D}(s)\sigma_0 \tag{2.3.9}$$

which leads to

$$\bar{\nu}(s) = \frac{\sigma_0}{\varepsilon_0} s\bar{\mu}_{creep}(s)\bar{D}(s) \tag{2.3.10}$$

where $\mu_{creep}(t)$ is the the negative ratio of the measured strains during the creep test.

The term $\frac{\sigma_0}{\varepsilon_0}$ corresponds to the modulus of the material for an infinitely short time (instantaneous application of the stress and strain response). As, amorphous polymers behave like glasses at very short times, $\frac{\sigma_0}{\varepsilon_0}$ can be measured as the glassy modulus, related to the glassy compliance $E_g = 1/D_g$. The relation (2.3.10) becomes:

$$\bar{\nu}(s) = \frac{1}{D_g} s\bar{\mu}_{creep}(s)\bar{D}(s) = E_g s\bar{\mu}_{creep}(s)\bar{D}(s) \tag{2.3.11}$$

Finally, the VPR for a creep test is given as the inverse Laplace transform of $\bar{\nu}(s)$:

$$\nu(t) = E_g \nu_{creep}(t) D(t) \tag{2.3.12}$$

The error in the measurement of the asphalt VPR from the correct equation (2.3.12) and from the negative ratio of the transverse and longitudinal strains $\nu_{creep}(t)$ during compressive creep is found to be up to 11% [Alanazi et al., 2019] and between 10% and 30% [Kassem et al., 2013] for unconfined specimens.

2.3.4 Strain under creep loading

Knowing the material VPR $\nu(t)$ (2.3.12), the transverse strain from a creep test can be obtain by replacing $\nu_{creep}(t) = \frac{\varepsilon_{xx}(t)}{\varepsilon_{yy}(t)}$ and $D(t) = \frac{\varepsilon_{yy}(t)}{\sigma_0}$, leading to:

$$\nu(t) = -E_g \frac{\varepsilon_{xx}(t)}{\varepsilon_{yy}(t)} \frac{\varepsilon_{yy}(t)}{\sigma_0} = -\frac{E_g}{\sigma_0} \varepsilon_{xx}(t) \tag{2.3.13}$$

where σ_0 is the creep stress. The transverse strains are then

$$\varepsilon_{xx}(t) = -\nu(t) \frac{\sigma_0}{E_g}. \tag{2.3.14}$$

CHAPTER III

MATERIALS AND METHODS

3.1 Materials

The objective is to measure the VPR and evaluate its influence on the web handling process with materials that are commonly used by the web handling industry. Three viscoelastic web materials have been chosen as representative of the level of simplicity or complexity commonly encountered in webs. The low-density polyethylene web, further referred to as **LDPE** (Fig. 5(1)), is considered perfectly isotropic and homogeneous. It represents an ideal case of isotropic linear viscoelasticity. This LDPE is compared to its anisotropic equivalent, a low-density polyethylene described as oriented, and referred to as **LDPEO** (Fig. 5(2)). The LDPE and LDPEO are purchased from Blueridge Films, Inc. (Disputanta, VA). Finally, a spun-meltblown-spun nonwoven, referred to as **NW** (Fig. 5(3)), represents a widely used and highly complex web. The NW is provided by Kimberly-Clark Corporation (Neenah, WI). NWs are heterogeneous materials formed by a network of bonded fibers on a macroscopic scale [Martínez-Hergueta et al., 2015]. Their heterogeneous structure leads to a challenging size-dependent and anisotropic mechanical behavior.

As often for webs, the LDPEO and NW are assumed orthotropic, that is they possess three planes of symmetry and their properties change along three orthogonal axes. As the thickness of a web is far smaller than the other dimensions, the web behavior is assumed constant in the thickness. Consequently, the strains are constant through the thickness and the use of 2D Digital Image Correlation (DIC) is relevant

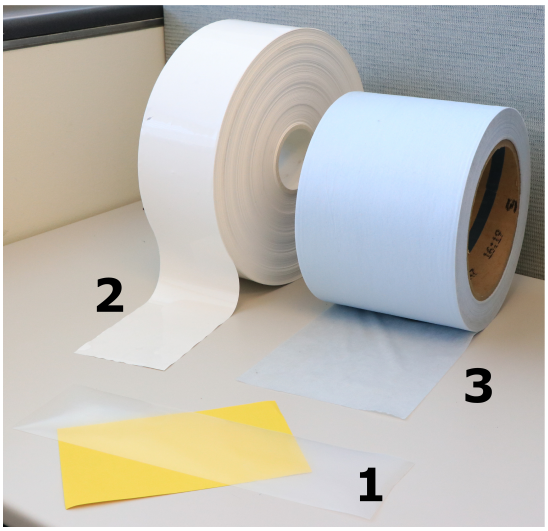

Figure 5: Web rolls of (1) the LDPE, (2) the LDPEO, and (3) the NW

to characterize web behavior. A more complete description of the DIC procedure is given in the following. We further assume that the main direction, *i.e.* the axis of orientation and higher stiffness, is along the Machine Direction (MD) of the web. This assumption will be confirmed experimentally.

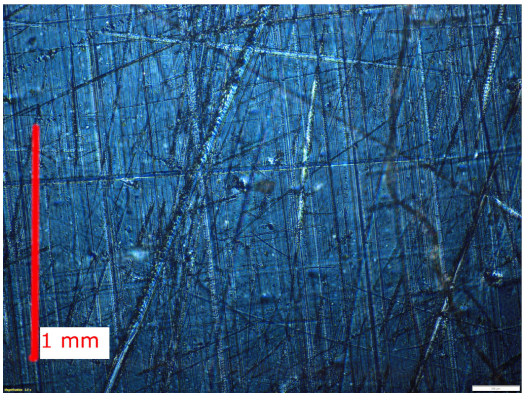

(a) LDPE

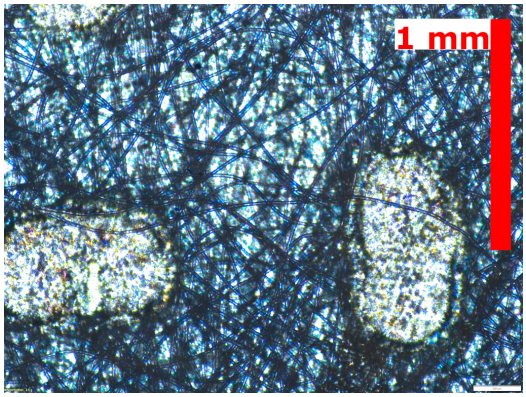

(b) NW observed under polarized light. The vertical is the MD direction.

Figure 6: Microscope views of LDPE and NW. The red line corresponds to 1 mm.

The LDPE and the NW have been observed with a microscope Olympus SC50 equipped with a lens $5x/0.10$ and an inverted polarized light. Due to its high opacity,

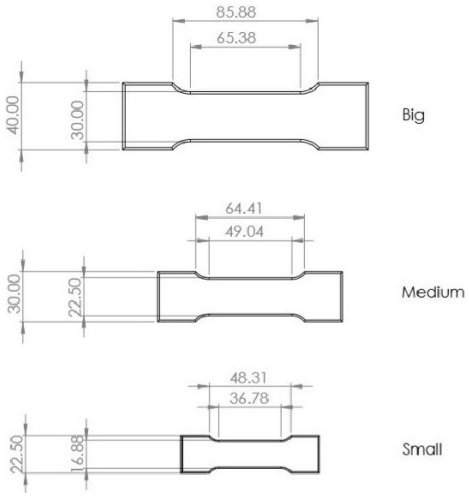

Figure 7: Specimen dimensions

the structure of the LDPEO could not be observed with the microscope. The LDPE structure presents a solid matrix (Fig. 6a). The NW is composed of fibers linked together at the bonding points through melting, visible on the image as the white oval marks (Fig. 6b).

3.2 Specimen Preparation

3.2.1 Cutting the specimens

Part of this study investigates the influence of specimen size on the VPR. We define three sizes for dumbbell specimens, all of aspect ratio 2.18 but of different dimensions. The exact dimensions are provided on Figure 7 and the specimens will be referred as 'Big', 'Medium', or 'Small' throughout the study.

The shape of each specimen has been 3D-printed as a model (Fig. 8a). In order to cut a specimen out of a web, the outline is first cleanly drawn with a marker directly on the web following the outside border of the model shape (Fig. 8b).The specimen is then cut with scissors and a paper trimmer. Once the specimen is cut, its dimensions (width and thickness) are measured at three different positions and the average is recorded.

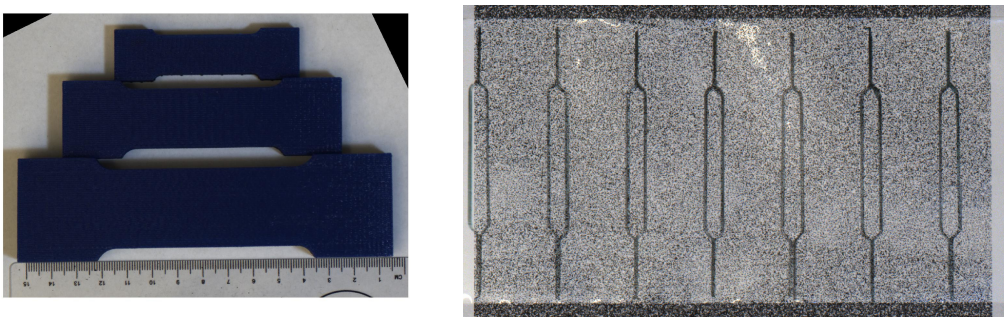

(a) Model shapes 3D printed (b) LDPEO specimens drawn

Figure 8: Drawing specimen shape.

3.2.2 Patterning

DIC is a widely-used and contact-less method to measure strains, making it a good option for the purpose of this study. Open-source softwares to perform DIC on acquired images are available and the method is easily implementable on common lab equipment. Others methods include the projection of a Moiré pattern instead of a painted pattern on the specimens or use of a strain gauge [O'Brien et al., 2007, Giovagnoni, 1994]. The latter is not a relevant option as the contact of a measuring tool with the soft specimen affects the accuracy of the measurements. In addition, Moiré patterns can't be used with transparent materials, such as LDPE.

In order to perform Digital Image Correlation (DIC), the specimens must be patterned, meaning a random homogeneous distribution of black spots must be fixed to the surface.

The pattern is either sprayed or printed on the specimens. For the sprayed pattern, the specimen is manually sprayed with a an air brush (Master Airbrush G233-set) filled with black India ink (Dr. Ph. Martins, Bombay Black). For the printed pattern, an inkjet printer is used to directly print black ink on the specimen (Fig. 9). The image printed is a random distribution of black spots of constant size generated in MATLAB.

(a) Ink Jet Printer (b) LDPEO specimens with printed patterns

Figure 9: Hardware used to draw and print the pattern.

The main difficulty with patterning is to distribute the black spots homogeneously on the surface while still keeping them random. For example, the pattern can be too dense (Fig. 10a) or too inhomogeneous (Fig. 10b) to provide a good basis for DIC. The printed patterning technique provides better patterns in terms of randomness and resolution, mostly because the size of the speckles is smaller and better controlled. However, printing is not appropriate on NW materials as they tend to absorb the deposited ink, resulting in small speckles coalescing.

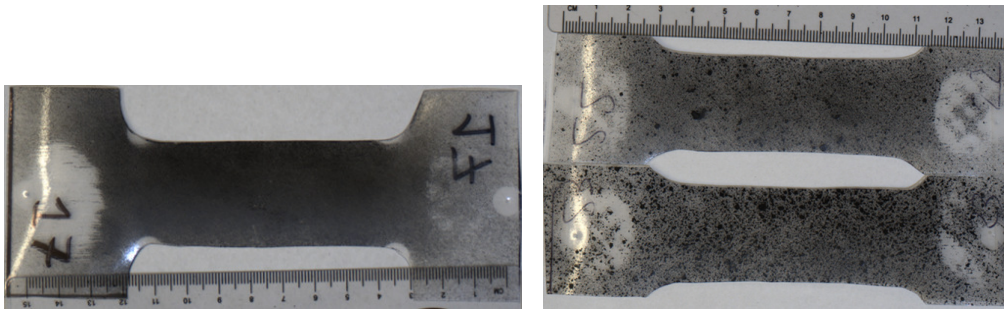

(a) Pattern too dark (b) Heterogeneous pattern

Figure 10: Coarse pattern on LDPE specimens

3.3 Mechanical testing

3.3.1 Uniaxial tensile testing

LDPE cast webs are assumed isotropic and hence the Young's modulus is independent of the direction. LDPEO and NW materials are anisotropic and their Young's modulus is expected to depend on direction. An additional question arose for the LDPEO. As the roll has been purchased without any manufacturing guarantee, it is possible that the preferred orientation of the material actually differs from the MD direction of the roll. In order to verify this assertion and to assess the main axis of the LDPEO roll, uniaxial tensile tests are performed on these webs.

Figure 11: DMA testing station

Uniaxial tensile tests are performed with a RSA-G2 apparatus (TA Instruments, Natwick, MA) on small rectangular specimens of dimensions 50mm x 9mm (Fig. 11). The tensile test is performed on 12 LDPE specimens to determine the average Young's modulus. LDPEO specimens oriented along eight angles with respect to the machine direction (MD) of the roll, 0°, 22.5°, 45°, 67.5°, 90°, 112.5°, 135° and 157.5° (Fig. 12) are tested. Six specimens are tested in each each orientation. The NW web

is measured along the MD and the cross machine direction CMD in order to verify the anisotropy of the material. 14 and 23 specimens are tested along the MD and CMD directions, respectively. The direction of the principal modulus for the NW is assumed to be either along the MD or the CMD direction of the web.

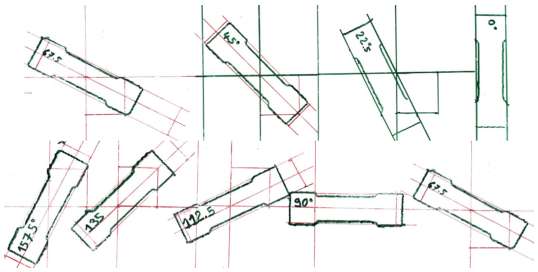

Figure 12: Orientation of the LDPEO specimens for tensile testing (MD = horizontal direction).

The specimens are stretched at a strain rate of 1 %/s at room temperature up to 100% engineering strain. The slope of the stress-strain curve for an engineering strain below 1.5 % determines the Young's modulus.

3.3.2 Glassy modulus measurement

The constant glassy modulus E_g quantifies the behavior of the material in the glassy domain, below the glass transition temperature, where the viscoelasticity is extremely low and effectively nonexistent. For LDPE, the glassy modulus E_g has been estimated at 650-700 MPa via molecular dynamics simulations [Yazdani et al., 2019]. We will use a value of 700 MPa for both the LDPE and LDPEO web in both orientations.

The glassy modulus can also be measured performing tensile tests at decreasing temperatures until a plateau is observed. As the behavior of specific NW webs has been less explored in the literature, we will directly measure E_g for the NW. Rectangular specimens of length 20 mm, width about 7 mm, and thickness 0.07 mm are placed in the RSA-G2 apparatus and stretched at 1 $\%/s$ until failure at 10°C, 0°C,

-10°C, -20°C, -31°C, -42°C, -52°C, and -62°C. The temperature is controlled with liquid nitrogen and room temperature air. The slope of the stress-strain curve for an engineering strain below 1.5 % determines the Young's modulus.

3.3.3 Stress relaxation tests

The stress relaxation and creep testing is performed on an Instron tensile machine (INSTRON 5960) equipped with a load cell of 500 N (Fig. 13). The specimens are gripped with specially designed and 3D-printed grips adapted to their large width. In addition, plastic grips avoid unnecessary damage to the specimen heads compared to metallic ones. The roughness of the grip surface resulting from 3D-printing was sufficient to avoid specimen slippage in the grips during testing.

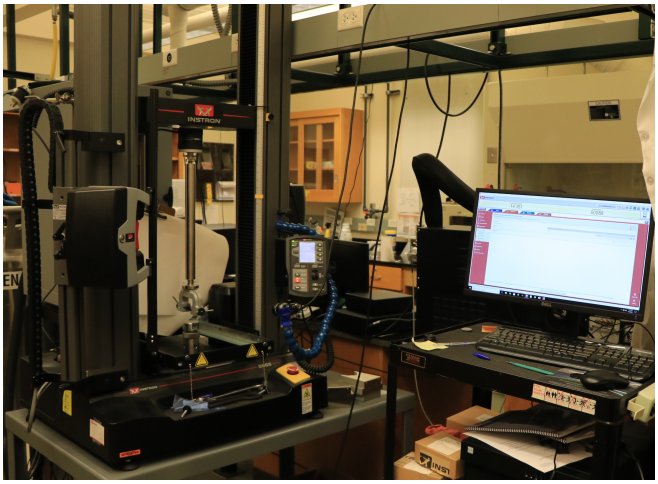

Figure 13: Instron testing station

A stress relaxation test measures the time-dependent response of the material to an instantaneous constant strain, commonly called a strain step. As no strain can physically be instantaneous, a relatively fast strain ramp and a hold are programmed in the machine. The strain increases to 5% for the LDPE and the LDPEO and 1% for the NW, at a strain rate of 10 %/s. The strain is then held for 20 min.

The level of strain hold, 5% for LDPE and LDPEO, and 1% for NW, has been

determined by preliminary testing as the maximum level attainable without creating instabilities in the web such as trough, wrinkling, or any out-of plane instability. It is essential for this test that the material remains in a small strain regime, where the viscoelasticity can be assumed linear and the strain remains two-dimensional. The DIC performed would loose meaning if the strains became three-dimensional. The specimen must remain planar for the DIC measurements to be credible.

3.3.4 Creep test

One difficulty of performing creep tests with standard tensile machines is that the test is load-controlled while the machine is displacement-controlled. The software controlling the equipment needs PIF parameters, gain setting parameters made from a proportional gains, an integral factor, and a lag filter, that are an equivalent to the common PID parameters. These parameters are used in a feedback loop for the machine to reach the targeted load at each step. These PIF parameters highly depend on the tested material properties. A preliminary study of the appropriate PIF parameters for each materials and orientation is performed. The proportional gains is obtained following the method proposed by Instron [Instron, 2013]. The integral gain and lag filter are determined by trial and error. The obtained PIF parameters are given in table 1.

Table 1: PIF parameters for each specimen category

	LDPE	LDPEO	LDPEO	NW	NW
	-	MD	CMD	MD	CMD
Proportional gain	0.0100	0.014	0.0150	0.03	0.01
Integral gain	1.1	1.3	1.3	1	1.07
Lag filter	0	200	200	200	200

A creep test measures the time-dependent response of a material to an instantaneous constant stress. The strain increases at a rate of 1%/s until the stress reaches 7 MPa for the LDPE, 2 MPa for the LDPEO, 0.5 MPa for the NW in MD, and 0.4 MPa for the NW in CMD. The stress is then held for 20 min.

Similarly to the strain level of the stress relaxation test, these stress levels have been chosen after preliminary testing as the maximum stress at which the material remains flat and in a small strain regime.

3.4 Digital Image Correlation (DIC)

3.4.1 Image recording

In order to perform DIC, images of the patterned specimens have to be recorded at small time intervals during deformation. One of the main difficulties in recording these images is to have the camera fixed in a position perfectly oriented facing the specimen surface. This problem has been solved by using a versatile lockline that allows positioning of objects in space and 3D-printing adaptors to attach it directly to the tensile frame.

During stress relaxation and creep tests, images of the specimen are recorded with a video camera (FLIR Blackfly S BFS-U3-50S5C) equipped with a flat-field lense (HR 35 mm/F1.8 85868 Edmund optics). To avoid any shadows on the specimen, two lights are positioned on each side of the camera (Fig. 14). White paper is placed behind the specimen to create a homogeneous background. The background is positioned to avoid the specimen shadow to be visible on the images. For a transparent material like the LDPE, a shadow behind the specimen would reduce the contrast of the black pattern with the white background.

Once the specimen and the camera are both positioned, a calibration picture is taken with a ruler on the side of the grip (Fig. 15). This calibration image will be

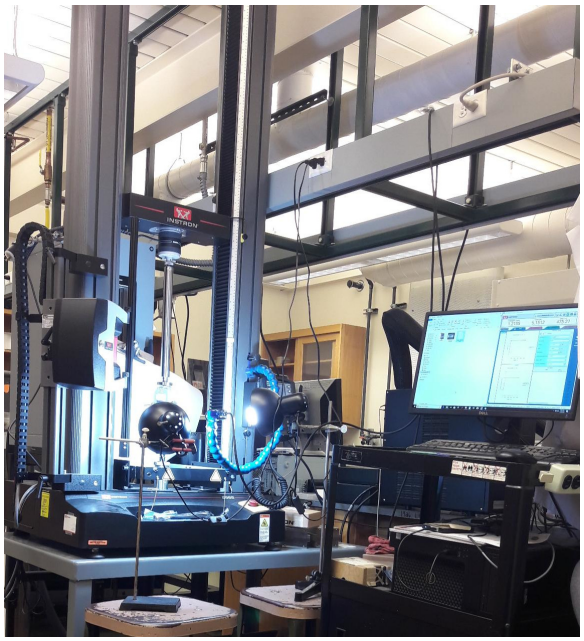

Figure 14: Set up for continuous recording of images during the test.

used to convert the DIC units from pixel to mm.

Figure 15: Calibration image recorded before the test.

The camera acquires images at a rate of 1 frames per second. Considering the limited strains observed during a stress relaxation or creep test, this frame rate represents a good compromise between measuring the strain variations and reducing the computing time of the subsequent DIC, as well as accommodating the limited rate transfer and computing capacities of the data acquisition system. To improve the

correlation, the contrast of the color images is increased by converting them to black and white in MATLAB.

3.4.2 Digital Image Correlation with Ncorr

The DIC is a contactless process to measure the strain on the surface of a patterned specimen. The DIC algorithm compares gray levels to estimate the displacement of each point of the pattern; a process commonly called image correlation. The displacement of the points $x_{i,0}$ from the initial frame to $t = 20$ s is computed in the subset, represented by the dash red circle (Fig. 16).

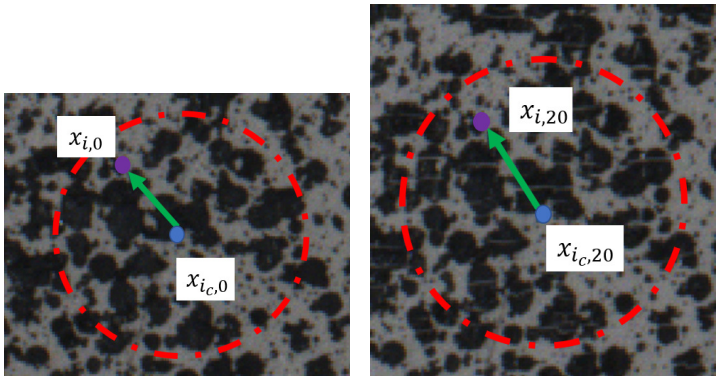

(a) Initial frame (b) Frame after 20 min

Figure 16: Relative displacement of two points of the pattern on a 'small' LDPE specimen. The red circle represent the subset.

The DIC analysis of the images is made with NCORR [Blaber & Antoniou, 2017]. The process in NCORR (Fig. 17) begins by loading the images, starting with the reference image corresponding to the initial or reference configuration. The initial configuration corresponds to the state of strain of the specimen at the end of the loading ramp. We select every other frame for the DIC study to reduce the computing time, that is one frame every 2 seconds. Because each test in this study contains 600 pictures, the images are loaded to the computer memory only when the algorithm

processes them ('Lazy' mode).

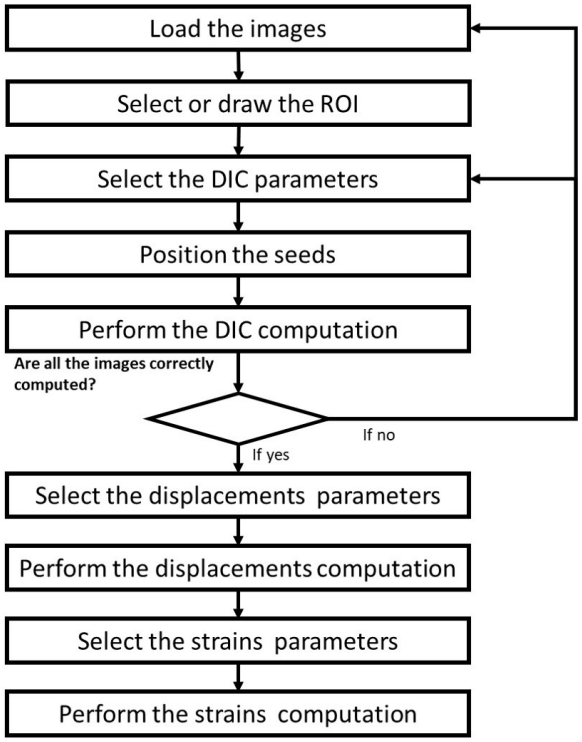

Figure 17: Flowchart of the computation with Ncorr.

The Region Of Interest (ROI) is hand-drawn on the specimen reference image as a rectangle (Fig. 18).

Figure 18: ROI drawn on the specimen in NCORR software.

The next step is to define the parameters of the DIC computation, namely the

subset radius, the subset spacing, the number of threads, and the use or not of the high strain analysis (Fig. 19a).

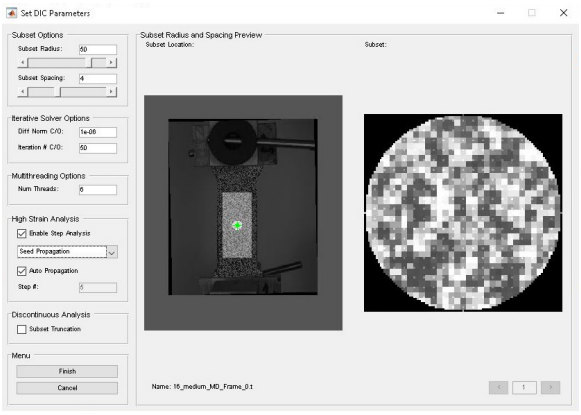

(a) DIC parameters

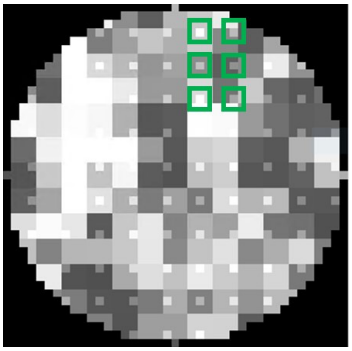

(b) The subset spacing is the distance between the points marked as green rectangles.

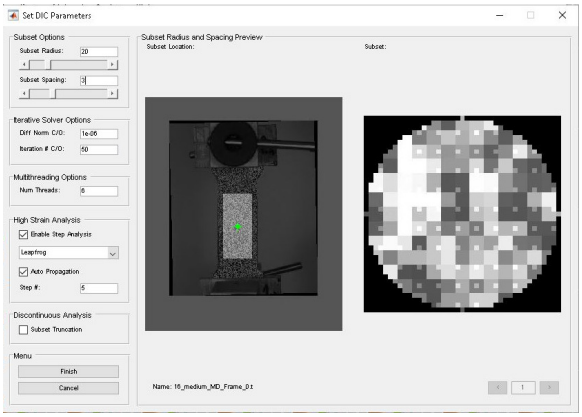

(c) Subset radius too low

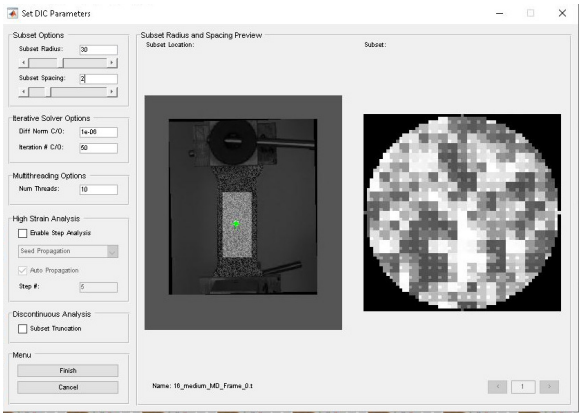

(d) Subset spacing too low

Figure 19: Selecting the DIC parameters, subset radius and subset spacing.

The subset radius is the most critical parameter of the computation. The objective is to use the smaller subset possible without increasing the error in the computed displacements to an unacceptable level. If the subset radius is set too low (Fig. 19c), the computation will return an error as the number of pixels in the subset is insufficient to correlate the pattern at different time steps.

The subset spacing (Fig. 19b) is the distance between the points where the compu-

tation is performed. The subset spacing strongly influences the computational time. If the subset spacing is too low (Fig. 19d), the computation will be time consuming without significantly increasing the accuracy of the results.

Both these parameters depend on the pattern and the image resolution. After preliminary trials, the subset radius is selected between 40 and 60 pixels. and the subset spacing was between 3 and 5 pixels.

The number of threads is the number of seeds positioned to initiate the computation on several cores. The hand positioning of the seeds limited our computation to 8 threats, with some tests processed with only one thread.

The high strain option updates the reference image and the ROI during the computation. By default, the computation was attempted without the high strain option. If the strains are too high to allow for the image correlation, the high strain option was included in the analysis. Two strategies are available in the software, 'Seed propagation' and 'Leap frog'. The 'Seed propagation' automatically update the reference image and ROI according to the DIC computation results. With the 'Leap frog', the reference image and DIC are updated at a fixed image frequency. The seed propagation strategy was favored in our processing, with the 'Auto propagate' option where seeds are automatically positioned by the software on the new reference image.

The next step is to position the seeds in the ROI. The number of seeds is determined by the number of threads. The seeds are positioned to reduce the number of intersections between domain borders while distributing the area equally among the seeds. One way to do it is to position them with a regular pattern (Fig. 20a), avoiding to intersect too many border where the errors can occurs (Fig. 20b).

Then, the image correlation is performed. Two of the main issues is the detection of a high correlation between two images by the algorithm or the inability of the algorithm to recover the pattern position on two consecutive images. Modifying the DIC parameters, such as the subset radius, and running another correlation generally

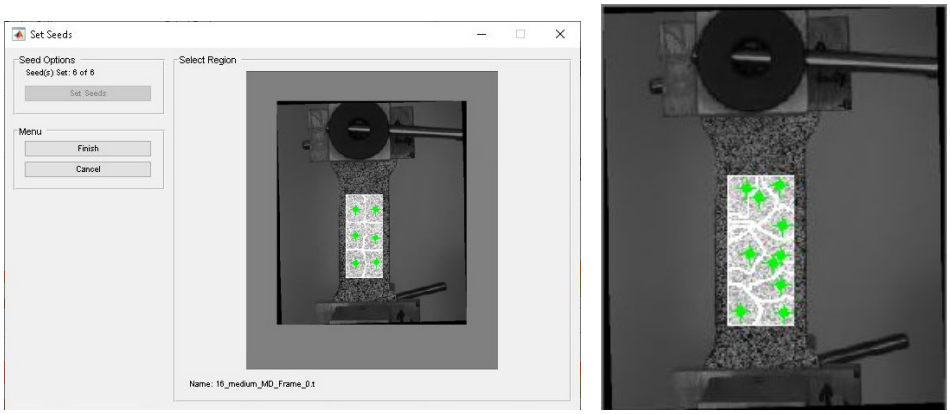

(a) Seeds correctly positioned (b) Seeds incorrectly positioned

Figure 20: Positioning of the seeds.

solves the issue.

As a result of the image correlation, the software computes the displacements and the corresponding strains. The conversion pixel-to-mm of the displacement values is performed with the calibration image recorded before the test (Fig. 15).

The strains computed are fitted to a local group of circular data points. The radius of this circle is called in NCORR interface the strain radius. The usual values used are between 5 and 10 with most of them close to 5 pixels. The displacements and strains at each points of the surface and each time step are saved in a .mat file to be post-processed with MATLAB.

3.5 Computation of the VPR

The strain in each direction is approximated by the median of the strain field over the ROI for each frame. The median is preferred to the mean as it is less sensible to outlier values, that is, in our study, strain heterogeneities. This operation can be time-consuming and this operation has been implemented in a parallel code to process several specimens simultaneously. The corresponding codes are presented in Appendix 8.4.

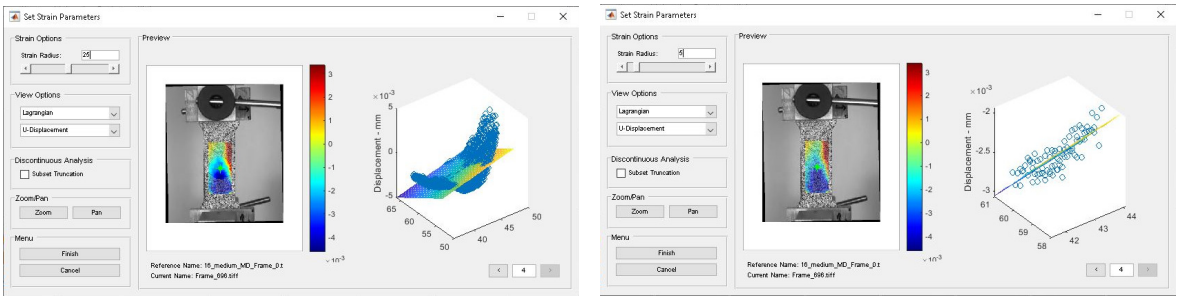

(a) Too large radius

(b) Correct radius

Figure 21: Setting of the strain radius. The blue points on the right graph should be as close as possible to the plane for a correct strain field.

The VPR is computed using the formulas developed in Chapter 2, equation (2.3.4) for the stress relaxation test and equation (2.3.12) for the creep test.

For the stress relaxation tests, the VPR is directly computed at each time step as the ratio of the transverse strain and the imposed axial strain. The imposed axial strain ε_0 is taken as the mean of the axial strain measured by the machine as the change in length over the initial length. The transverse strain is the median of the transverse strain at each point over the whole specimen (codes in Appendix 8.4).

For the creep tests, axial and transverse strains are computed as the median of the strain distribution. The specimen compliance is computed as the axial strain, measured by the machine from the change in length, divided by the constant stress taken as the mean of the measured stress. The glassy compliance is either measured or taken from the literature as described in the mechanical testing section.

Finally, a mathematical model (Equ. (3.5.1)) is fitted on the obtained time-dependent VPR in order to quantitatively compare the results.

$$\nu(t) = \nu_s e^{-t/\tau_s} + \nu_l e^{-t/\tau_l} + \nu_\infty \tag{3.5.1}$$

where ν_∞, ν_s, and ν_l represents real constants and τ_s and τ_l are the relaxation times of

the Poisson's ratio. The fit is performed in MATLAB using a least-square algorithm with the function lsqcurvefit (code in Appendix 8.4). The coefficients ν_s and ν_l are constrained to be of the same sign so that the exponential terms do not cancel each other. τ_s is maintained between 5 s and 200 s as the short-term relaxation time, and τ_l is kept above 200 s. Consequently, ν_s and τ_s represent the short-term viscoelastic behavior, ν_l and τ_l the long-term viscoelastic behavior, and ν_∞ the equilibrium PR. ν_∞ is set at $\pm 15\%$ of the mean of the last 20% points of the curve.

To facilitate the fitting process, the starting point of the fitted data is selected between 0 s and 20 s. Right after the loading ramp, the results are often scattered and more difficult to fit. Eliminating these points can facilitate the fitting process.

If one coefficient ν_s or ν_l is lower than 10^{-4}, the corresponding term is not used in the following statistical analysis, meaning both ν_s and τ_s or both ν_l and τ_l would be excluded.

3.6 Statistical analysis

The influences of the experimental conditions on the VPR, as represented by the model in equation (3.5.1), are systematically explored with targeted analyses of variances (ANOVAs). The experimental conditions are the independent factors of the ANOVAs:

1. the material: LDPE, LDPEO, or NW,
2. the orientation: MD or CMD,
3. the size of the specimen: 'Small', 'Medium', 'Big'.

As will be demonstrated in chapter IV and discussed in chapter V, the creep tests do not lead to relevant values of the VPR. Consequently, the statistical analysis is only performed on the stress relaxation results.

In all analyses, the effect of an independent factor is deemed significant if the corresponding p-value is below $p_{lim} = 0.1$.

Because the LDPE is isotropic while the LDPEO and the NW are anisotropic, it is not possible to perform a global ANOVA considering orientation. Indeed, orientation will have very different effect according to the material studied. Similarly, the size of the specimen is not expected to influence the parameters of the model in a similar way for each material because of their different level of heterogeneity. Consequently, we perform targeted ANOVAs over specific conditions. As a note, the sample size is not large enough to allow for an analysis including all independent parameters and their interactions, which would avoid such decomposition of the analysis.

3.6.1 Influence of the material

The influence of the material, LDPE, LDPEO, and NW, is evaluated using an ANOVA for each orientation 'MD' and 'CMD'. Only specimens of size 'medium' are included. As the LDPE is isotropic, the behavior of the web is the same in 'MD' and 'CMD' directions. LDPE results are considered as 'MD' for the 'MD' ANOVA and 'CMD' for the 'CMD' ANOVA.

3.6.2 Influence of the orientation

The influence of the orientation is evaluated using an ANOVA including only anisotropic materials LDPEO and NW, with specimen of size 'Medium' (Table 2).

3.6.3 Influence of the specimen size

The influence of the size of the specimen is evaluated using a separate ANOVA for each material, including all orientations when relevant. The three specimen sizes 'Small', 'Medium', and 'Big' are considered. The size 'Big' is not included for the LDPEO as the number of specimens was too low to perform an ANOVA. The table

Table 2: Parameters of the ANOVA evaluating the influence of the orientation. Specimen size 'Medium'.

Material	Orientation
LDPEO	MD
NW	CMD

3 presents the factors of the ANOVA.

Table 3: Parameters of the ANOVA evaluating the influence of the specimen size. The ANOVA is repeated for each material. * Orientation is not included for the LDPE ANOVA. ** The size 'Big' is not considered for the LDPEO ANOVA.

Orientation*	Size
MD	Small
CMD	Medium
	Big**

CHAPTER IV

RESULTS

4.1 Material Properties

4.1.1 Young's modulus and verification of orientation

The Young's modulus of each material has been performed through tensile tests, which allows to verify the orientation of the LDPEO web and the anisotropy of the NW web.

The average Young's modulus for the LDPE is 160 MPa. An example of the measured stress-strain curves is presented in figure 22b.

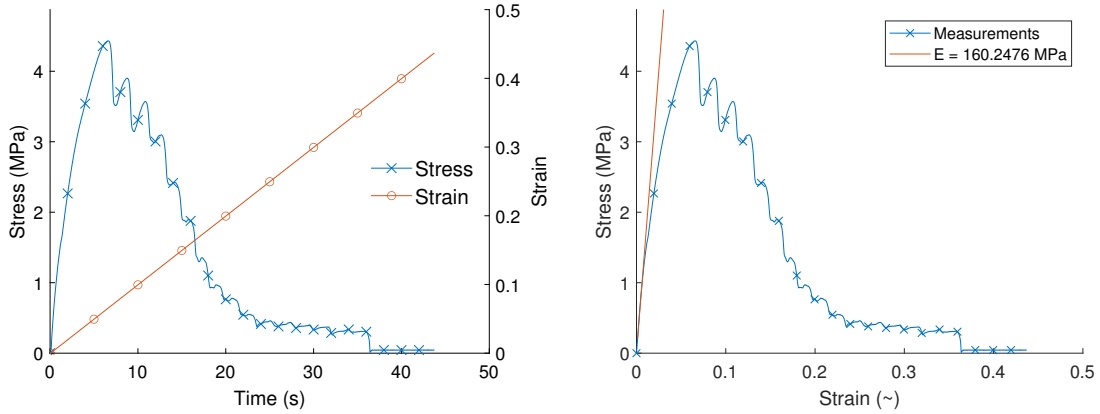

(a) Stress and strain during a uniaxial tensile test, LDPE. The specimen size is 50mm x 9mm.

(b) Computation of the Young's modulus.

Figure 22: Stress and strain measured during a uniaxial tensile test to acquire the LDPE Young's modulus.

To verify the orientation of the LDPEO, a series of tensile tests have been performed along varied directions. Results indicate that the maximum modulus is obtained along the 0°direction, confirming our initial assumption that the main axis of the web was in the MD direction. The average Young's modulus measured for the LDPEO is 162.5 MPa in the MD direction and 79.9 MPa in the CMD direction (Fig. 23a).

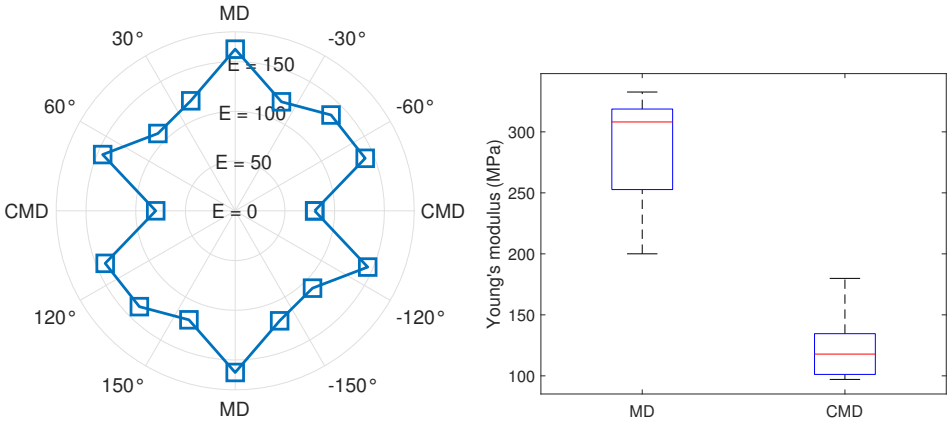

(a) Young's modulus function of the LDPEO orientation (units MPa)

(b) Young's modulus of the NW (MPa)

Figure 23: Young's modulus of the LDPEO and NW in various directions.

The NW was tested in the suspected MD and the CMD direction. The average Young's modulus of the NW is 287 MPa for the MD and 122 MPa for the CMD direction (Fig. 23b). The difference between the Young's modulus along the MD and the CMD direction confirms the NW is anisotropic.

4.1.2 Relaxation modulus and creep compliance

The stress relaxation and creep tests are direct measurements of the relaxation modulus and creep compliance of each material (Fig. 24). The relaxation modulus $E(t)$ of each material (Fig. 25a) characterizes its time-dependent behavior as directly measured by a stress relaxation test.

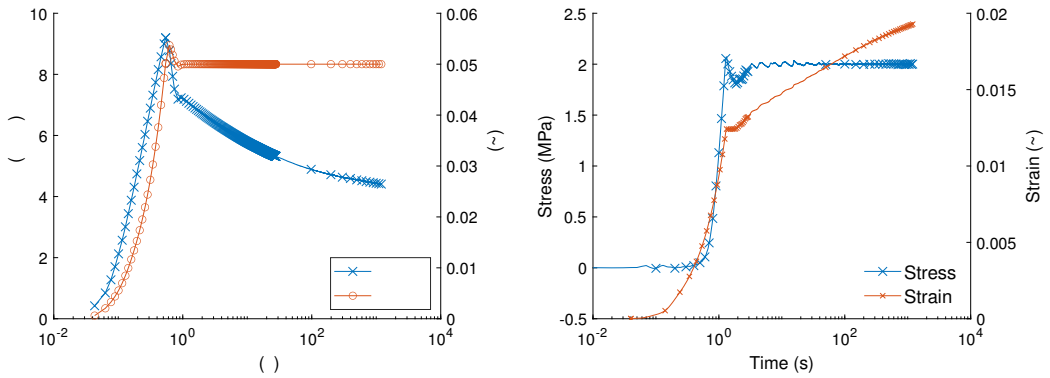

(a) Stress relaxation, LDPEO specimen, 'Medium', CMD direction.

(b) Creep, LDPEO specimen, 'Medium', CMD direction.

Figure 24: Example of stress-strain results from a stress relaxation or creep test.

Similarly, the creep compliance $D(t)$ characterizes the time-dependent behavior of the material as directly measured by a creep test (Fig. 25b). This compliance is necessary to compute the 'real' VPR $\nu(t)$ from a creep experiment.

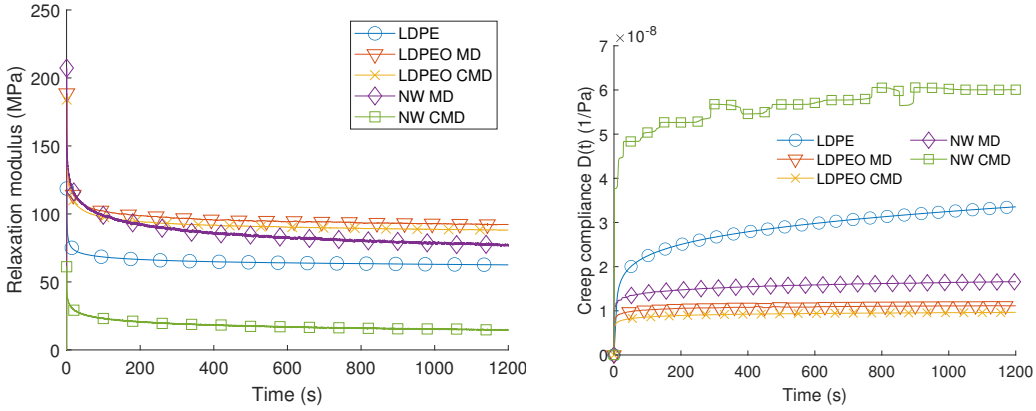

(a) Stress relaxation

(b) Creep compliance

Figure 25: Relaxation modulus and Creep compliance. The results presented are for a 'Medium' specimen size.

4.1.3 Glassy modulus for NW

From the literature, the glassy modulus of the LDPE was estimated at 700 MPa [Yazdani et al., 2019]. We will assume a similar value for the LDPEO glassy modulus along the principal axis. The glass transition temperature of the LDPE is -120°C [Balani et al., 2014].

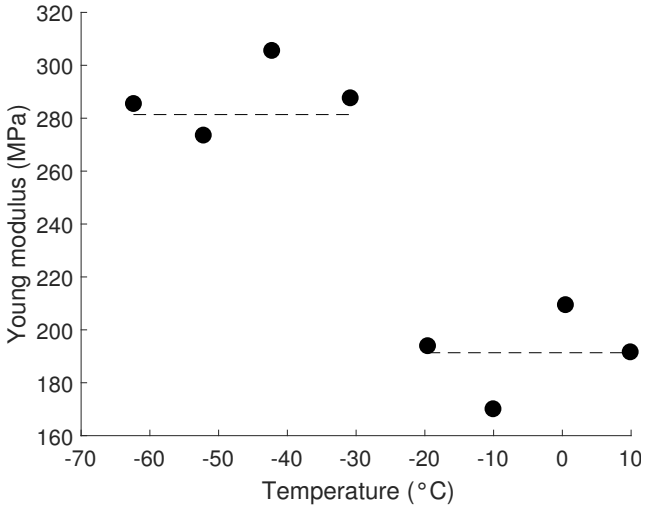

Figure 26: Young's modulus of the NW MD as a function of temperature.

The Young's modulus of the NW in MD shows a distinct increase at a transition temperature around -25°C (Fig. IV.5). The data exhibits two plateaus around -25°C. The glass transition temperature reported for the polypropylene is -18°C [Balani et al., 2014], which is very similar to what has been measured here. The dashed lines correspond to the mean of the values for each plateau. The glassy modulus of the NW MD is estimated at Eg = 281.37 MPa. The Young's modulus measured below the glass transition and the one measured at room temperature are very close. In addition, this series of measurements according to temperature indicates a room temperature modulus much lower than the one previously measured in section IV.1.1. This incoherence in the data indicates at least one of these measurements is wrong.

4.2 Longitudinal and transverse strain fields

4.2.1 LDPE

The strain fields of a LDPE specimen during a stress relaxation test (Fig. 27) and during a creep test (Fig. 28) are fairly homogeneous. This homogeneity in the strain field confirms the homogeneity of the LDPE.

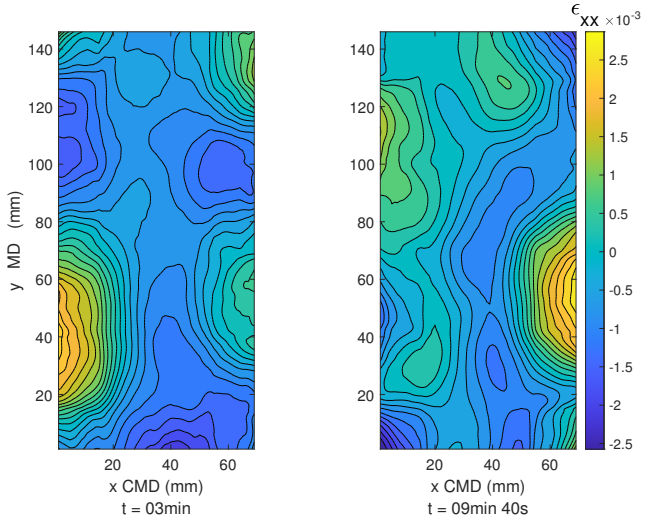

(a) Strain along the x axis, ε_{xx}

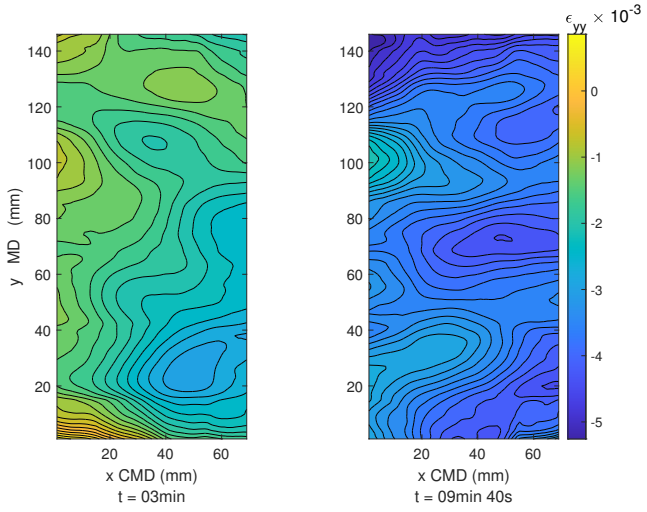

(b) Strain along the y axis, ε_{yy}.

Figure 27: Strain field during a stress relaxation test, LDPE size 'Medium', loading applied along the MD.

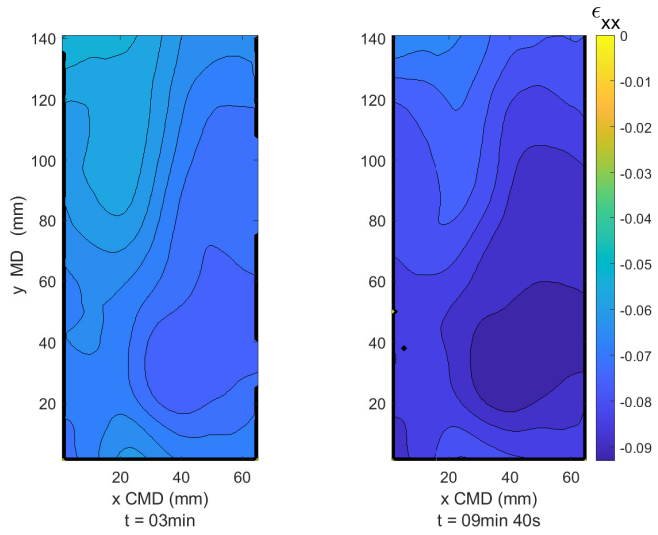

(a) Strain along the x axis, ε_{xx}

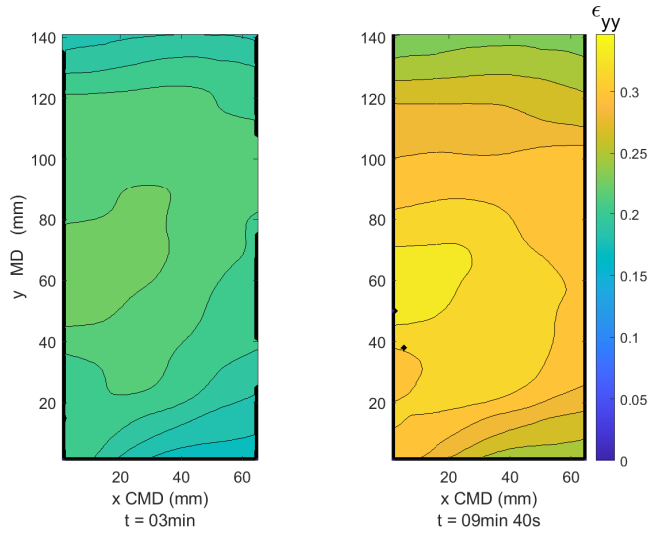

(b) Strain along the y axis, ε_{yy}

Figure 28: Strain field during a creep test, LDPE size 'Small'.

4.2.2 LDPEO

The plots (Fig. 29), shows an example of the full-field strain map of a medium LDPEO specimen oriented along the MD orientation during a creep test. These figures correspond to the test 13min and 02s after the beginning of the test.

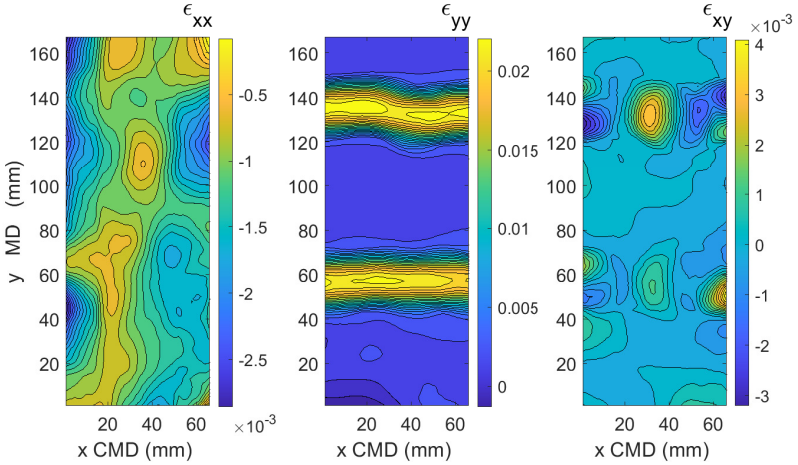

Figure 29: Strain fields during a creep test, LDPEO size 'Medium', 'MD' direction, at t = 13 min 2 s.

The means of ε_{xx} and ε_{yy} (Fig. 29) are -1.17×10^{-3} and 6×10^{-3}, respectively, while the mean of ε_{xy} is 0.125×10^{-3}. The shear strains ε_{xy} is much smaller than ε_{xx} and ε_{yy} and can be neglected.

The standards deviations of ε_{xx} and ε_{yy} are 4.08×10^{-4} and 7.2×10^{-3}, respectively (Fig. 30). The strain ε_{yy} exhibits a significantly wider distribution than ε_{xx}. The strain ε_{xx} spreads from -3×10^{-3} to 0.5×10^{-3} while the strain ε_{yy} spreads from 0 to 2.5×10^{-2}.

The lowers values of ε_{xx} are mainly located at the border of the specimen. The ε_{yy} distribution exhibits a strong peak around 0.0015 and a second lower peak around 0.0215. The second peak corresponds to the high strains bands observed (Fig. 30b). The presence of high strain bands is a recurring behavior for the LDPEO web.

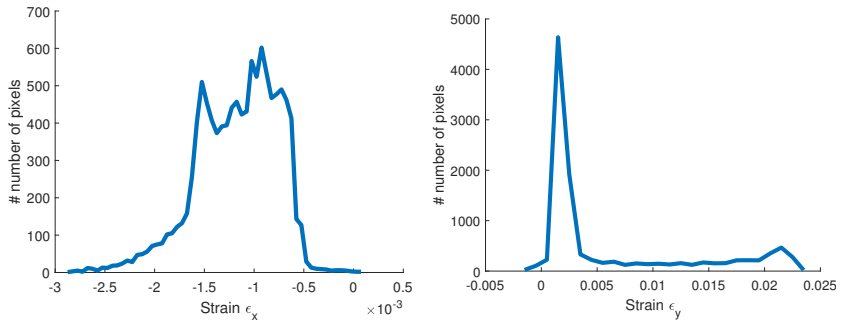

(a) ε_{xx} distribution (b) ε_{yy} distribution

Figure 30: Strain distribution during a creep test, LDPEO size 'Medium'.

They appear in similar manner for a LDPEO specimen loaded in the CMD direction (Fig. 31). The bands are oriented in the CMD.

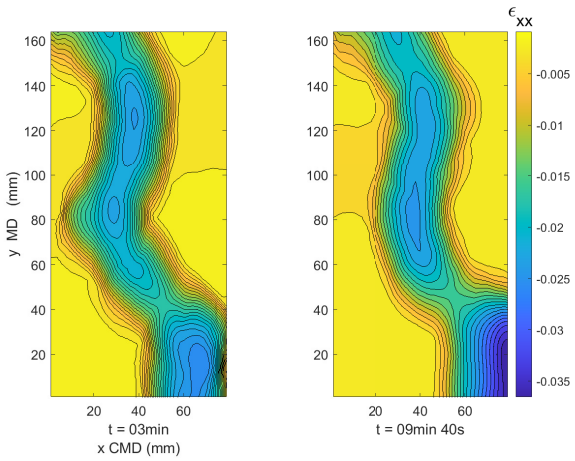

Figure 31: ε_{xx} strain field during a creep test, LDPEO size 'Medium', CMD direction.

This strain gradient indicates that the LDPEO, which was assumed to be homogeneous, is either heterogeneous or exhibits variations in thickness. The variation of strain ε_{yy} presents a large amplitude. If the thickness was the only cause of the heterogeneity, the thickness variations would probably have been measured with a micrometer. In either case, the material cannot be assumed perfectly homogeneous in terms of mechanical behavior.

4.2.3 NW

Similarly the NW specimens exhibit strain heterogeneities during stress relaxation and creep tests. The number and position of these high-strain bands can vary with time throughout the test (Fig. 32). The high-strain bands appear to be oriented perpendicularly to the applied load (Fig. 33) and we suppose they are the direct result of the heterogeneity of the NW web.

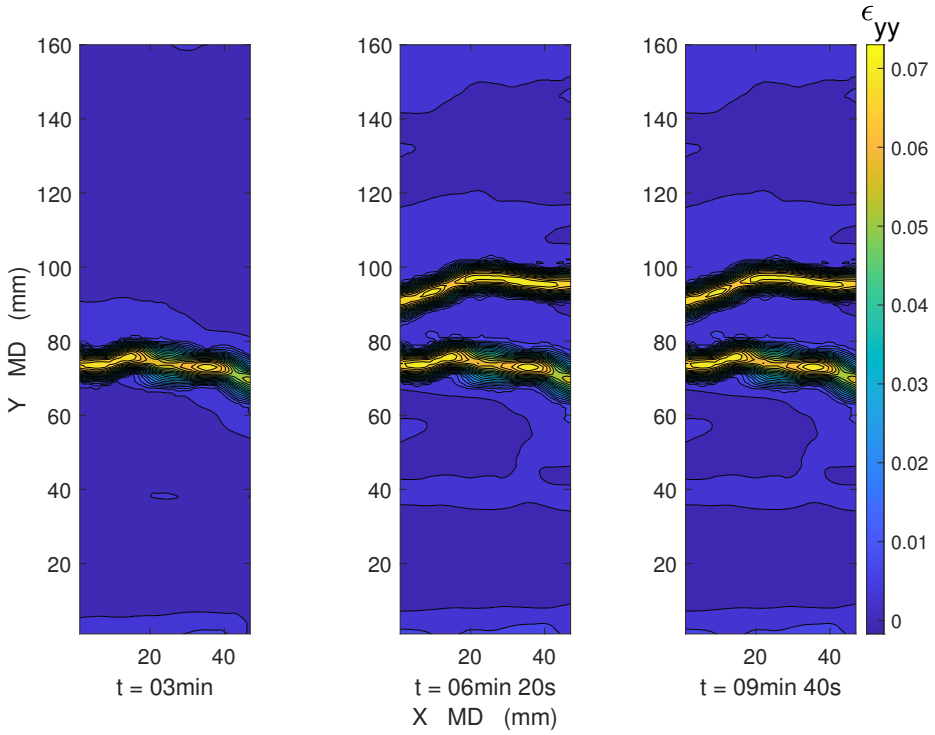

Figure 32: ε_{yy} strain field during a creep test, NW, 'Medium', CMD.

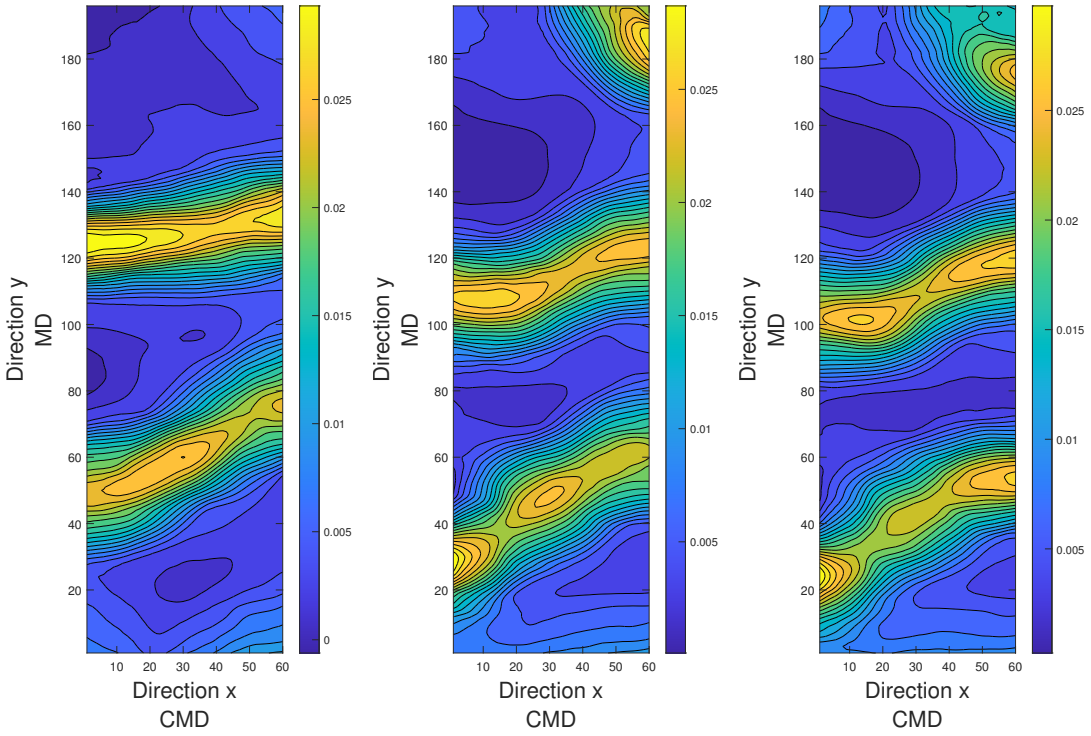

(a) $t = 1.6$ minutes (b) $t = 3.3$ minutes (c) $t = 4.9$ minutes

Figure 33: ε_{xx} strain field during a creep test, NW, 'Medium', MD.

4.3 VPR results

4.3.1 VPR computation

The strain fields are processed to obtain the longitudinal and lateral strains of the specimen (Fig. 34). The negative strain along the x-axis is the contraction due to the Poisson effect. Following the method described in Chapter III, the VPR is computed from these strains values (Fig. 35).

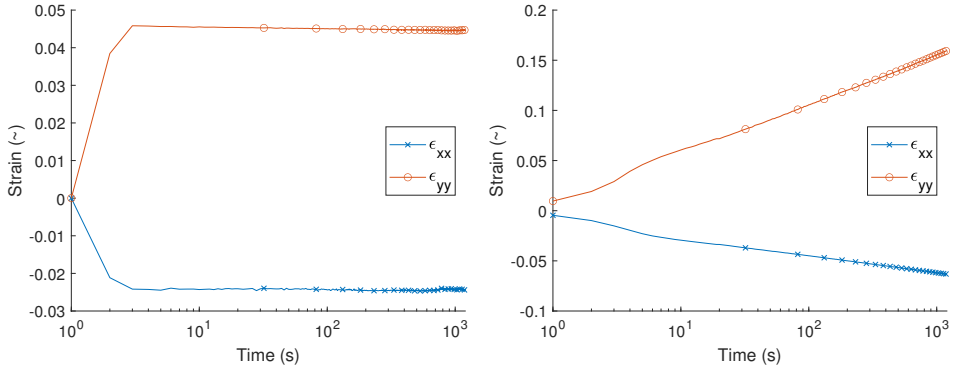

(a) Longitudinal and lateral strains during a stress relaxation test, LDPE 'Small'.

(b) Longitudinal and lateral strains during a creep test, LDPEO 'Big', MD.

Figure 34: Total longitudinal and lateral strains.

The VPR increases with time for both tests and is well represented by the two-term exponential model.

4.3.2 Model goodness of fit

Equation (3.5.1) is fitted on the experimental VPR results. Examples of VPR obtained for stress relaxation and for creep show that the model composed of two exponential terms is appropriate to represent the time evolution of the VPR (Fig. 35).

The goodness of fit is quantified by the squared norm of the residual $R = \sum_i (Y_{i,fitted} -$

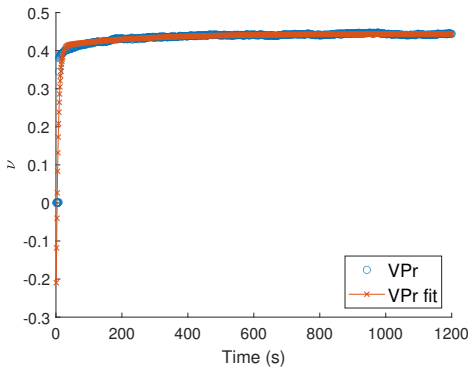

(a) VPR from Stress relaxation, NW, 'Big', MD.

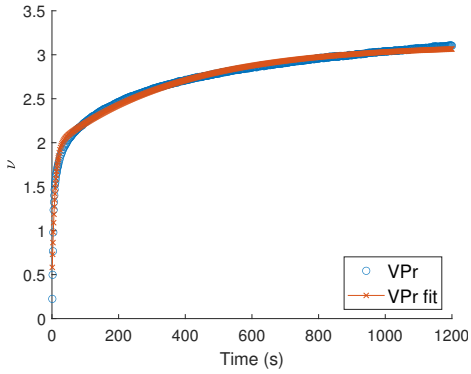

(b) VPR from Creep, LDPEO, 'Big', MD.

Figure 35: Computed VPR ν_{xy} through time and fitted model.

$Y_{i,exp})^2$ computed by MATLAB (Fig. 36a). R dramatically increases for a small number of specimens, see as an example Fig. 36b. The extremely high value of R is the direct result of scattered experimental data.

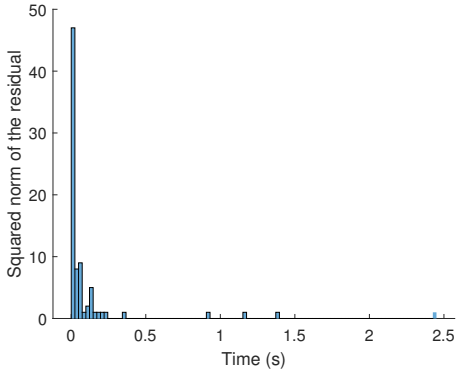

(a) Distribution of the squared norm of the residuals for all the VPR. Most values are below 0.0245.

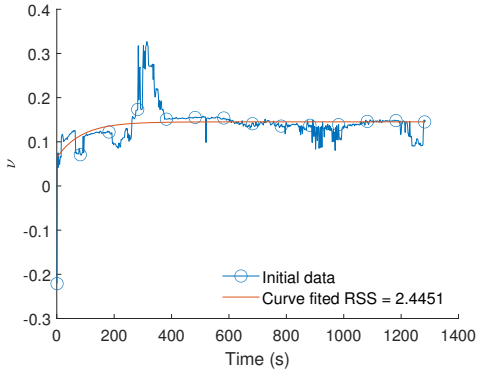

(b) Worst fit in stress relaxation, $R = 2.4451$, LDPEO, 'Medium', CMD.

Figure 36: Goodness of the fit.

A comparison of a 'good' and a 'bad' fit is given in figure 37. The difference between both curves is the stability of the VPR with time. The badly fitted curve

presents oscillations with time impossible to represent with the model used.

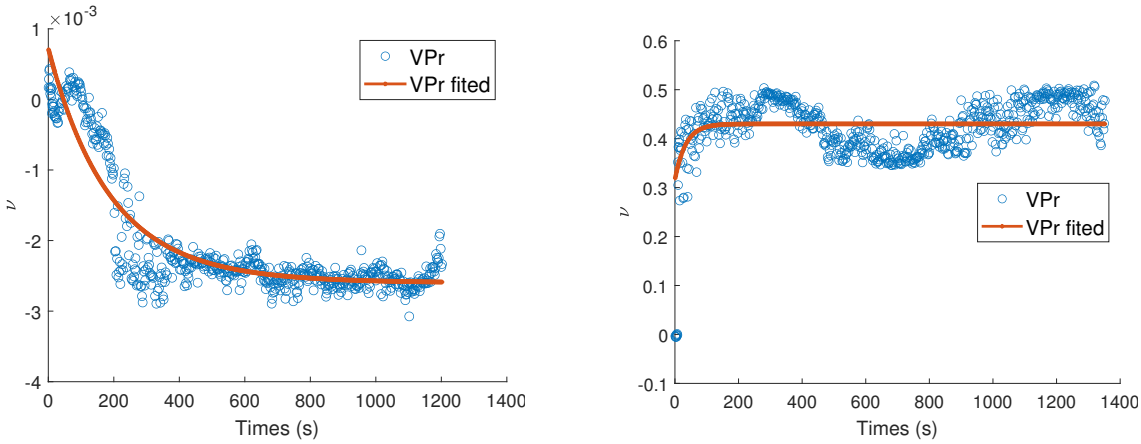

(a) VPR correctly fitted, 'Small' LDPEO CMD. $R = 7.29^{-5}$.

(b) Coarse VPR fit, 'Small' NW MD. $R = 1.39$.

Figure 37: Comparison between a fine and a coarse VPR fit.

4.3.3 Resulting VPR from stress relaxation

The final VPR model corresponds to the average of the coefficients obtained for each material and orientation (Table 4).

Table 4: Final VPR model from stress relaxation.

Materials	Orientation	ν_s	τ_s	ν_l	τ_l	ν_∞
LDPE		0.0052	24.8738	0.0090	368.6432	0.3880
LDPEO	MD	0.0011	14.7350	−0.0108	858.3905	0.4317
LDPEO	CMD	0.0048	59.8181	0.0093	1.1566×10^3	0.3986
NW	MD	−0.0472	40.1956	−0.0313	1.5569×10^3	0.2964
NW	CMD	−0.0104	19.1566	−0.0311	970.0617	0.1224

The plot of the VPR, for each material and orientation, is presented in figure 38.

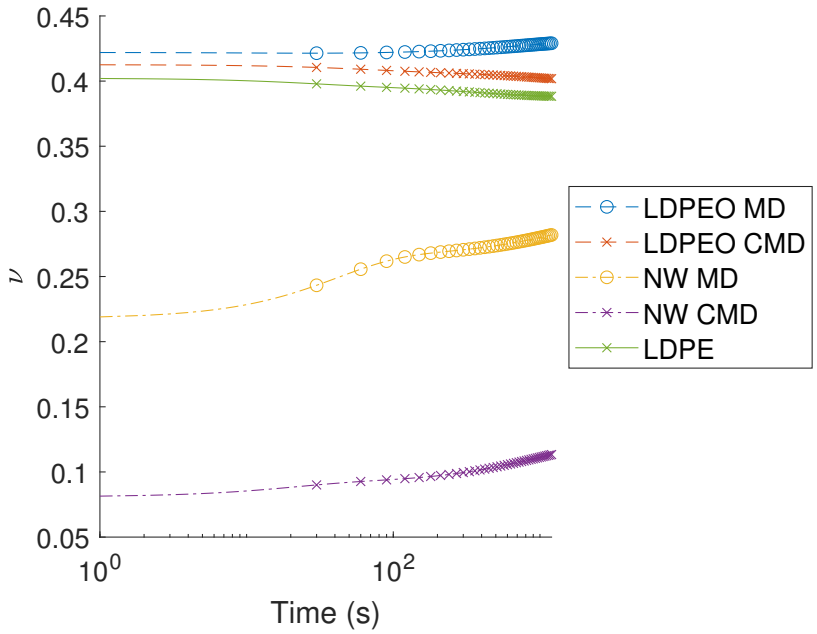

Figure 38: Final VPR models

4.3.4 Resulting VPR from creep

A similar general model is computed from the creep results. The value of each parameter is the mean of the coefficients for each orientation and material (Table 5).

Table 5: Final VPR model from creep.

Materials	Orientation	ν_s	τ_s	ν_l	τ_l	ν_∞
LDPE		0.02137	26.58524	−0.38196	7.0206×10^3	0.97880
LDPEO	MD	−0.2250	50.28841	−0.14363	596.8039	0.49036
LDPEO	CMD	−0.2055	42.6277	−0.1154	1.2831×10^3	0.4922
NW	MD	−0.4029	13.5865	−0.5087	571.3819	0.5338
NW	CMD	−1.0203	34.5180	−0.5494	676.1842	1.2445

The plot of the VPR obtained from creep is presented in figure 39.

Interestingly, if we focus on the ν_∞ values, the LDPEO presents values of 0.49 in both orientations, the LDPE ν_∞ unrealistically equals 0.98, and the NW ν_∞ equals

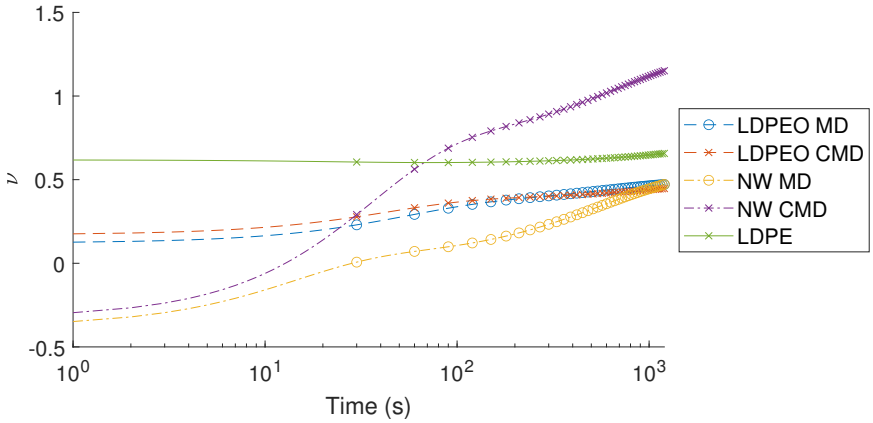

Figure 39: VPR according to time from creep

0.53 in MD and 1.24 in CMD. The LDPE VPR reaches $\nu(t = 1200s) = 0.66$ at $t = 1200s$. The difference between $\nu(t = 1200s)$ and ν_∞ is due to a high long relaxation time, τ_l, allowing for some variation of $\nu(t)$ at long times past 1200 s.

Finally, the coefficients ν_∞ from stress relaxation and creep are presented in figure 40 for comparison.

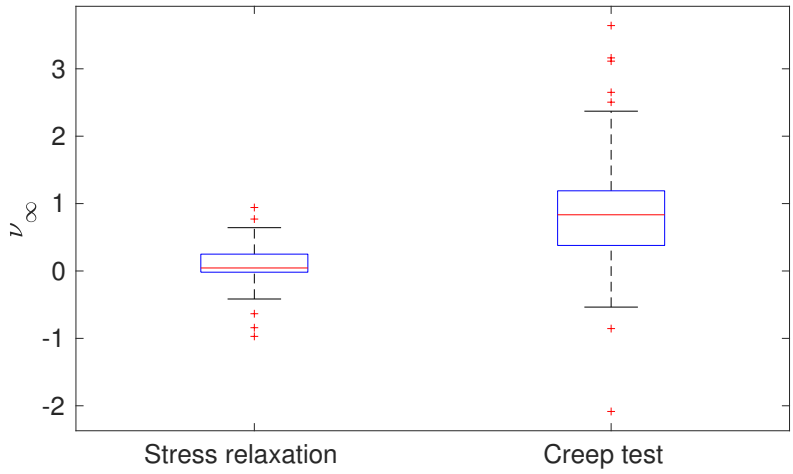

Figure 40: Distribution of ν_∞ from stress relaxation and creep.

CHAPTER V

DISCUSSION

5.1 Influence of the test

The VPR obtained from creep presents some unphysical values for the LDPE, an isotropic material. We will discuss this in the following comparing the equilibrium VPR values, namely ν_∞. The equilibrium value ν_∞ depends on the test, the material, and its orientation (Fig. 41).

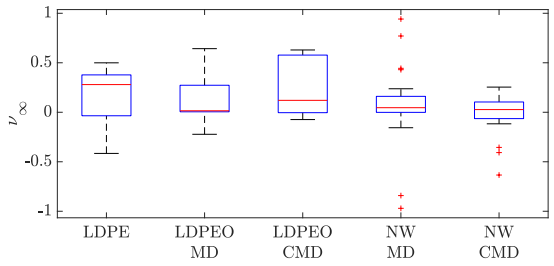

(a) Stress relaxation.

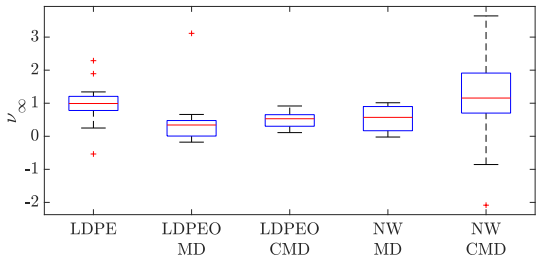

(b) Creep.

Figure 41: VPR equilibrium values ν_∞ according to material and orientation.

The coefficient ν_∞ in creep shows a high variability for the NW MD and CMD,

although less in MD. Measuring the NW VPR is difficult because it is a heterogeneous material. While a higher variability is expected for the NW compared to other materials, ν_∞ from stress relaxation does not exhibit such high standard deviations. Ultimately, the values of ν_∞ should be similar after processing of the data according to the equations presented in chapter 2. This proves untrue: the mean ν_∞ from stress relaxation is 0.027 while the mean ν_∞ from creep is 1.156 for the NW.

The unrealistic value $\nu_\infty = 1$ is obtained from creep for the LDPE. One experimental difficulty encountered with the LDPE was that the ink tends to crack when the specimen is stretched. As the pattern changes during the experiment, the strain may be overestimated by the DIC procedure.

The values of the VPR from creep for the LDPEO look coherent with respect to the values from stress relaxation using a value of E_g around 100 MPa. However, this means the glassy modulus would be lower than the one measured at room temperature, which would also not be realistic. Using a higher value and realistic value of E_g would lead to a higher VPR no longer similar to the value measured during the stress relaxation test.

Globally, creep tests have been found less reliable than stress relaxation tests for the following reasons:

- The data is more scattered in a creep test, especially at short times as the apparatus is using a PID procedure to regulate the load. The data are less 'stable' during a creep test, as is discussed below.

- It is almost impossible to measure the low values of strains at very short times using a creep test, due to the time necessary for the apparatus to regulate the load.

- Because this study is performed on webs and not on bulk materials, we are limited to low stress and strain values in order to remain in the linear viscoelastic

domain and maintain a two-dimensional specimen.

- As the creep strain is generally higher than the stress relaxation strain, some issues arise with the pattern maintaining its integrity through the deformation. The ink tends to crack when the specimen is stretched. As the pattern changes during the experiment, the strain may be overestimated by the DIC procedure.

- The creep processing method to obtain the VPR $\nu(t)$ relies on add-on measurements such as the creep compliance $D(t)$ and the glassy modulus E_g, which adds to the global experimental error.

Although some studies have directly measured the ratio of the strains to evaluate the VPR by DIC [Farfán-Cabrera et al., 2017], none have actually used the analytical method proposed here and compared the results with the VPR from stress relaxation.

In the literature, two methods have been used to measure the 'real' VPR from creep data. The first method computed the VPR during a creep experiment by solving an integral equation [Theocaris, 1964, Tschoegl et al., 2002]. The second method measured other time-dependent functions, such as the viscoelastic bulk modulus, to indirectly determine the VPR [Delin et al., 1995]. The main difficulty of these methods is reaching adequate accuracy of the measurement. An accurate measurement requires several decimal precision [Lu et al., 1997]. We did not implement these methods because current experimental technologies allow us to optically measure the 2D strains in the specimen. The procedure employed also avoids any approximation during the integration.

Another issue is the intrinsic instability of the measurement, that has been observed previously [Tscharnuter et al., 2011a]. The VPR during creep was measured for polymers, fluoroelastomer, neoprene/chloroprene, and ethylene-propylene-diene monomer by DIC using a dead weight [Farfán-Cabrera et al., 2017]. However, the VPR was only measured after the installation of the dead weight and the loading

ramp, ≈ 16 s, once the standard deviation of the strain decreased. This greatly limits the possibility of characterizing the material at short times. In our creep experiment, the load was applied during a few seconds and the VPR computed as soon as the ramp ended. This was necessary as the loading rates in web handling are relatively fast and only considering times past 20 s would be reducing the range too much. Optimization methods have been suggested as a way to deal with this experimental instability [Tscharnuter et al., 2011a]. The creep data has been optimized using stress relaxation data. Although the results are smoother, the creep data is still scattered and the authors note that the influence of the amount of smoothing might not be negligible.

We will discuss in the next sections the results of the ANOVA performed on the VPR models obtained from stress relaxation experiments only, determining which factors influence the time-dependent behavior.

5.2 Influence of the material

The results of the ANOVA test for the influence of the test and the materials for the MD and CMD orientations are presented in the table 6. The p-values resulting from the ANOVA are presented in the following tables. When a factor is deemed to have a significant effect, i.e. $p_{value} < p_{lim}$, the corresponding p-value is written in red. The header of the columns indicates the factor tested.

5.2.1 Equilibrium value ν_∞

Surprisingly, the equilibrium value ν_∞ is not significantly dependent on the material (Table 6) as the p-values are both above 0.1. We observe a large standard deviation of ν_∞ for the LDPE MD, which is probably influencing the statistical significance of any difference between materials (Fig. 42a). Similarly, although the median values seem significantly different, ν_∞ in CMD exhibits very large standard deviations compared

Table 6: ANOVA p-values for the influence of the material, MD and CMD.

	Material MD	Material CMD
ν_s	**0.07662**	0.55770
τ_s	0.28029	**0.00226**
ν_l	0.32117	**0.05065**
τ_l	**0.02999**	**0.03480**
ν_∞	0.45195	0.21100

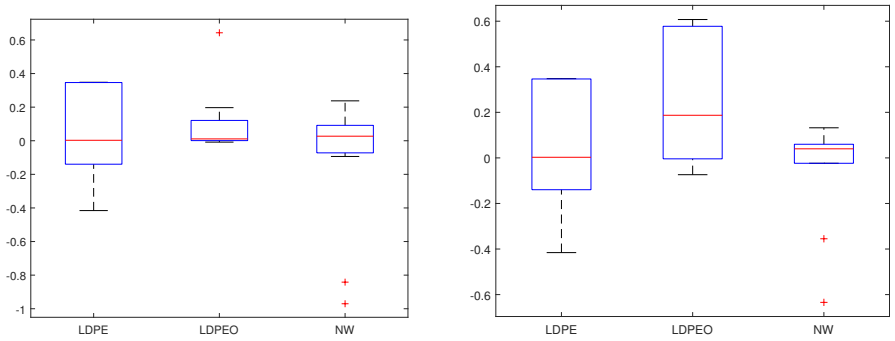

(a) MD ν_∞ (b) CMD ν_∞

Figure 42: ν_∞ as a function of the material.

to the median for LDPE and LDPEO (Fig. 42b). We attribute this unexpected behavior to the fact that we are testing webs and not bulk materials.

The LDPE and LDPEO VPR models present a similar behavior. The VPRs are fairly flat and decrease with time, with values between 0.4 and 0.45. In the literature, the LDPE VPR is reported as a monotonically increasing function with values between 0.45 and 0.46 after 1200s [Delin et al., 1995]. This value has been measured with a significantly smaller longitudinal strain (0.2% and 0.3 %), although this should not theoretically influence the VPR of a linear viscoelastic material. The VPR for three polymers stays in the range of the VPR values reported, between 0.39

and 0.52 [Farfán-Cabrera et al., 2017]. Consequently, the values reported here for the LDPE and the LDPEO are consistent with previous studies.

As a side note, the applied strain has been shown to influence the values of the VPR [Delin et al., 1995, Bauer & Farris, 1989] for non linear materials. The materials in this study are supposed to remain linear so the applied strain should not influence the VPR. The maximal strain is 1% for the NW against 5% for the LDPE and LDPEO. Using a higher strain for the NW would allow to test all the webs in identical conditions but this low value was selected to avoid damage and instability, that is to remain in the small strain linear viscoelastic region of the mechanical behavior. Since the ANOVA actually showed that ν_∞ is relatively material-independent, we may tentatively conclude that the applied strain is not significantly influencing the VPR here.

5.2.2 MD

The results for the MD orientation show a correlation between the material and the short time amplitude ν_s as well as the long time relaxation time τ_l (Table 6).

The coefficients of the model for each material are presented in figure 43. The NW presents a wider distribution in the MD direction for amplitudes and relaxation times but the mean values are fairly similar. According to the ANOVA results, the absolute short-time amplitude ν_s is significantly higher for the NW MD, leading to an influence of the material on this coefficient. On the other hand, τ_l is significantly higher, indicating a late increase of the VPR but of low amplitude. In the NW, a significant portion of the lateral contraction happens earlier than in the LDPE and LDPEO but the equilibrium value reached is similar.

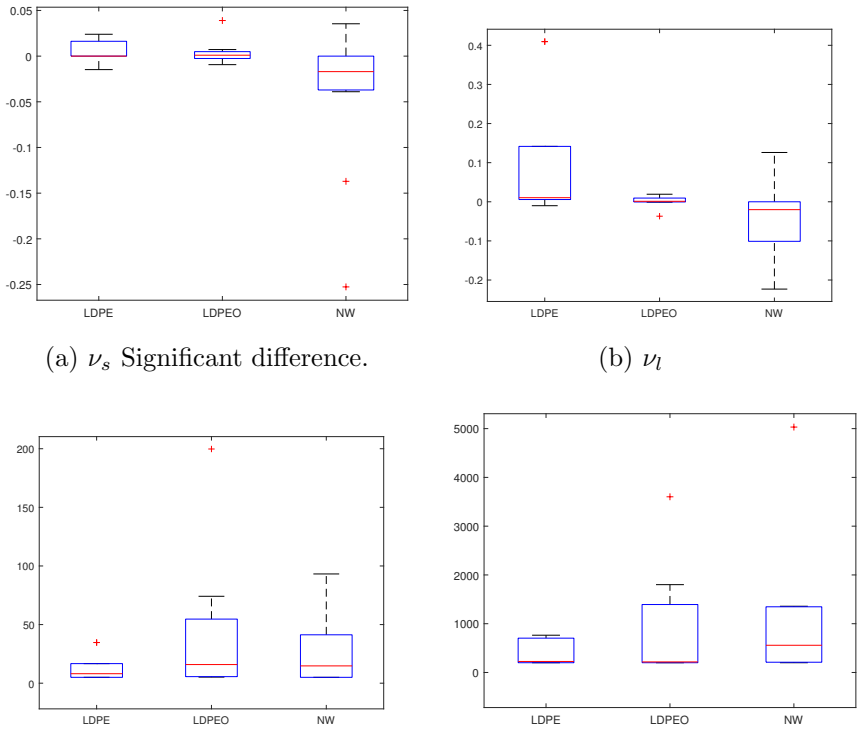

(a) ν_s Significant difference.

(b) ν_l

(c) τ_s (s)

(d) τ_l(s) Significant difference.

Figure 43: Model coefficients as a function of material in MD.

5.2.3 CMD

The material significantly influences the short and long relaxation times as well as the long-time amplitude in the CMD (Table 6). The material influences the long relaxation time in both directions. This indicates first that the time-dependent behavior is material-dependent. It also indicates that our measurement of the long-time behavior is probably more accurate than the short-time behavior.

In general, the coefficients of the model in CMD present a wider standard deviation than in MD (Fig. 44).

The short relaxation time of the LDPEO is significantly higher than the one of the LDPE. Similarly, the short-time amplitude is slightly higher, although not significantly. At long times, the difference between LDPE and LDPEO is not significant. This suggests the anisotropy of the material mainly influences the short-time behav-

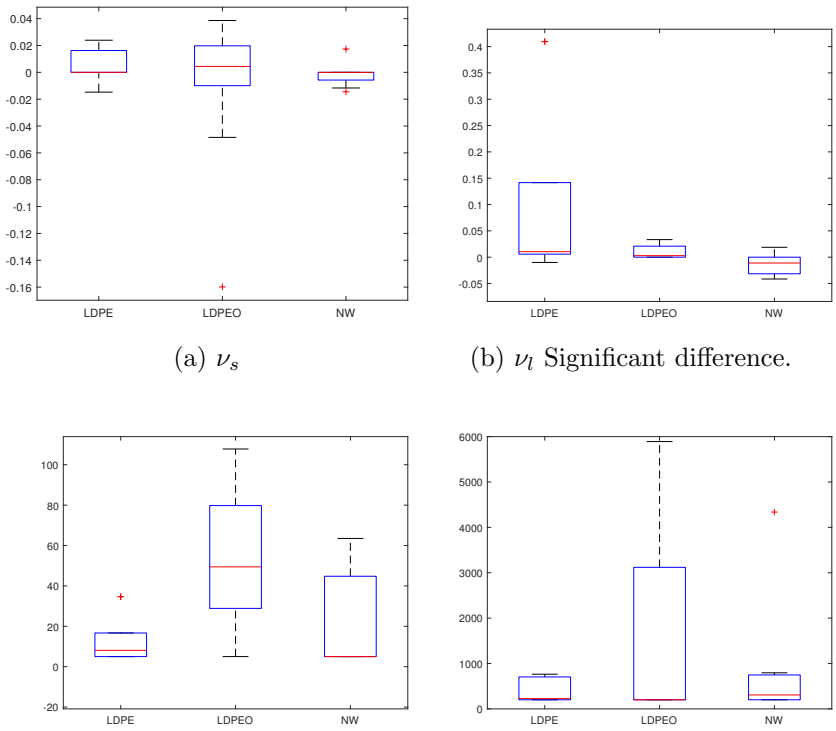

(a) ν_s

(b) ν_l Significant difference.

(c) τ_s (s) Significant difference.

(d) τ_l (s) Significant difference. Outliers not plotted

Figure 44: Model coefficients as a function of material in CMD.

ior.

The significant differences in the long time behavior mostly result from the NW behavior. Both absolute ν_l and τ_l are higher for the NW, indicating a delayed increase of the VPR with time. This is attributed to the peculiar structure of the NW, leading to longer relaxation phenomena.

5.2.4 Conclusion

Due to their structural differences, these webs exhibit various deformation mechanisms, which control the time-dependent VPR. The LDPE and LDPEO are bulk semi-crystalline polymers. Their mechanical behavior depends on the ratio between the amorphous and crystalline phases [Sperling, 2005]. The fibrils in the crystalline

and amorphous parts constitute the backbone of the material and resist any deformation. The amorphous phase alone opposes a lighter resistance to the deformation once the crystalline structure begins to deform [Sperling, 2005]. In addition, the crystalline structure is oriented in the LDPEO.This explains the difference in the short time amplitude for the VPR in each orientation.

Finally, rather than being a bulk material, the NW is an assembly of fibers, which leads to relaxation phenomena at a higher scale, translating to longer relaxation times. During tensile testing, bond damage strongly influences the fiber reorganization process. The number of bonds connecting the fibers depends on the orientation [Chen et al., 2016a, Martínez-Hergueta et al., 2015].

5.3 Influence of orientation in anisotropic materials

According to the ANOVA, the orientation does not significantly affect the coefficients of the model (Table 7).

Table 7: ANOVA p-values for the influence of orientation on model coefficients.

	Material	Orientation
ν_s	0.30623	0.38990
τ_s	**0.03303**	0.87895
ν_l	**0.00822**	0.33626
τ_l	**0.06573**	0.26052
ν_∞	0.29841	0.44549

The plots of each model parameter according to material and orientation confirm the lack of significant difference between MD and CMD (Figs. 45, 46, and 47).

There are however known differences between the deformation mechanisms in MD and CMD for the LDPEO and NW webs. For the LDPEO, the crystalline structure is

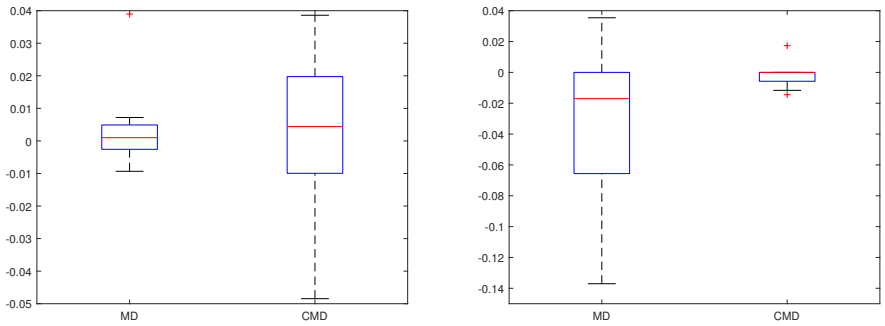

(a) ν_s LDPEO. Outliers not plotted.

(b) ν_s NW. Outliers not plotted.

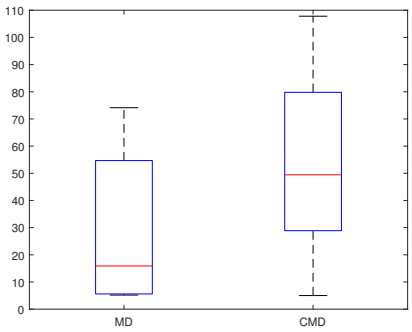

(c) τ_s LDPEO. Outliers not plotted.

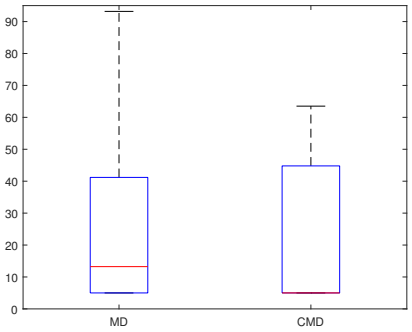

(d) τ_s NW. Outliers not plotted.

Figure 45: Short-time coefficients according to orientation.

already oriented. In MD, the fibrils will be the backbone of the materials to resist to any deformation while in CMD, the amorphous phase alone will resist the deformation [Sperling, 2005]. In the NW, the orientation depends on the orientation of the fibers. This orientation is usually characterized with a fiber orientation distribution function. In MD, once the bonds break, the fibers begin to stretch. In CMD, the fibers begin to stretch and reorganize before the bonds break [Martínez-Hergueta et al., 2015].

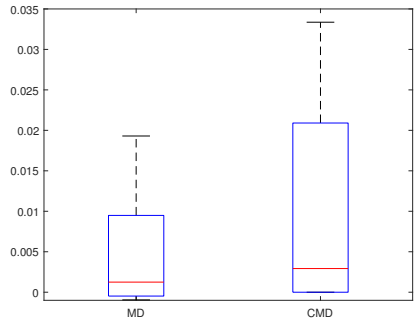

(a) ν_l LDPEO. Outliers not plotted.

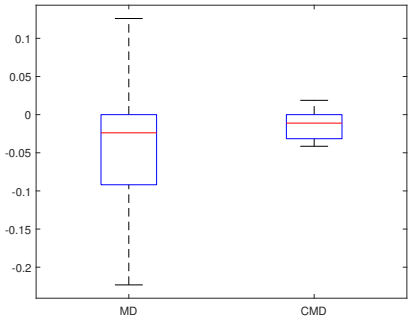

(b) ν_l NW.

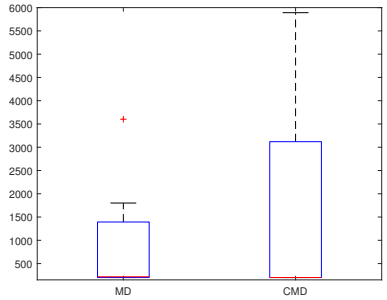

(c) τ_l LDPEO. Outliers not plotted.

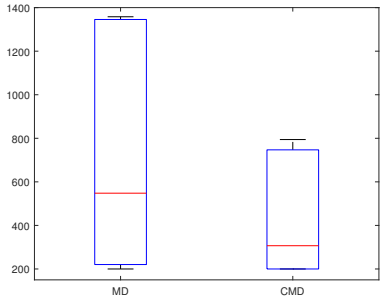

(d) τ_l NW. Outliers not plotted.

Figure 46: Long-time coefficients according to orientation.

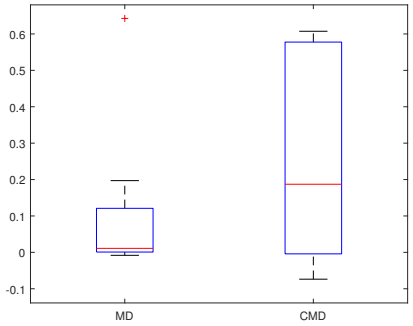

(a) ν_∞ LDPEO

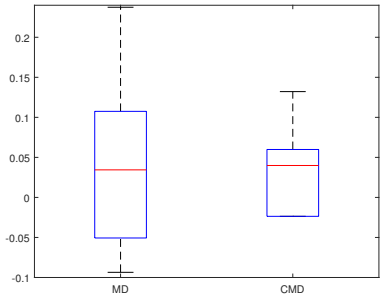

(b) ν_∞ NW. Outliers not plotted.

Figure 47: Distribution of ν_∞ according to the orientation for the LDPEO and the NW.

5.4 Influence of the specimen size

The results of the ANOVA detailing the influence of the specimen size on the model coefficients are presented in tables 8, 9, and 10, for the LDPE, LDPEO, and NW, respectively.

5.4.1 LDPE

Table 8: ANOVA p-values for the influence of specimen size on VPR model coefficients for the LDPE.

	size
ν_s	0.4848
τ_s	0.5615
ν_l	0.3405
τ_l	0.3980
ν_∞	0.1096

As expected, the specimen size has no influence on the model coefficients for the LDPE VPR. As the LDPE is a homogenous material, it should remain size-independent for all intrinsic material properties. This is what is observed here.

5.4.2 LDPEO

In LDPEO, the specimen size significantly influences the long-time amplitude ν_l. The short-time amplitude and long relaxation time seem similar for the sizes 'Small' and 'Medium' (Fig. 48). The short relaxation times present a wide distribution which prevents assessing significant differences between the sizes although the 'Medium' specimens seem to exhibit a higher short relaxation time τ_s.

Table 9: ANOVA p-values for the influence of specimen size on VPR model coefficients for the LDPEO.

	Orientation	Size
ν_s	0.5427	0.96938
τ_s	0.1734	0.76752
ν_l	0.74427	**0.0000**
τ_l	0.3274	0.63883
ν_∞	**0.07443**	0.30665

The strain bands measured during the test show a strong heterogeneity in the strain field (Fig. 29 and 31). The heterogeneity of the strain field is caused by a local heterogeneity in the material. It is interesting to notice that the bands recorded in the NW are wider than the ones in the LDPEO.

The LDPEO structure is composed of a row nucleated structure with twisted lamellae. The presence of high strain bands oriented along the CMD orientation (Fig. 29 and 31) suggests that the heterogeneity would be in the density of twisted lamellae. The zones with less twisted lamellae would be subject to more contraction than other zones [Zhang et al., 2004].

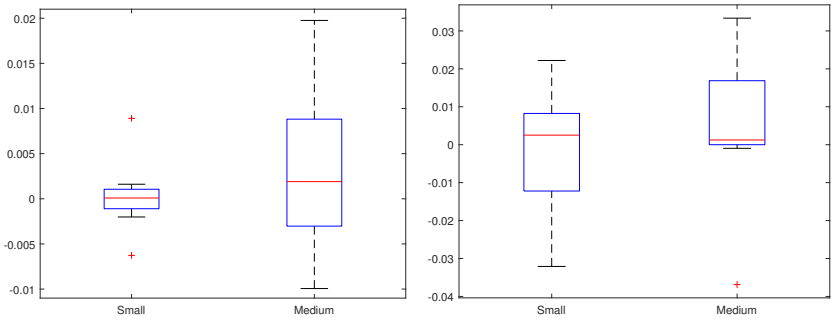

(a) ν_s. Outliers not plotted.

(b) ν_l Significant difference.

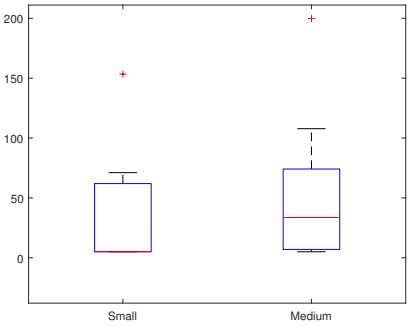

(c) τ_s (s)

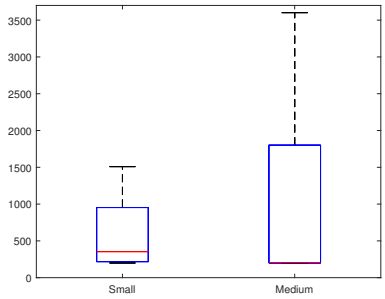

(d) τ_l (s). Outliers not plotted.

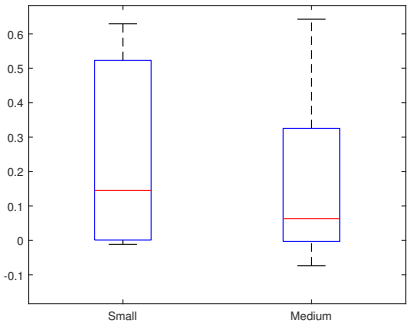

(e) ν_∞

Figure 48: Model parameters as a function of specimen size for the LDPEO.

5.4.3 NW

The ANOVA results for the NW show an influence of specimen size on the long relaxation time τ_l only (Table 10). Since the NW is a highly heterogeneous material, the specimen size was expected to influence most parameters of the model.

Table 10: ANOVA p-values for the influence of specimen size on VPR model coefficients for the NW.

	orientation	size
ν_s	0.13173	0.61463
τ_s	0.17939	0.23892
ν_l	0.61596	**0.08835**
τ_l	0.8373	0.86631
ν_∞	0.94622	0.19610

Further examination of the values indicate that the lack of influence of the specimen size is mostly due to the high standard deviation of each coefficient, as expected from a heterogeneous material (Fig. 49). Although the number of specimens has been increased for the NW compared to the LDPE and LDPEO, it seems it was not high enough to counteract the effect of the heterogeneity.

The absolute short- and long-time amplitudes seem to increase with specimen size, logically indicating higher VPR variations for larger specimens. In addition, the long relaxation time seems to increase with the size of specimen, indicating larger relaxation movements. Interestingly, ν_∞ seems to remain fairly constant, actually remaining size-independent.

Finally, the standard deviation of ν_s, τ_s, and τ_l is much higher for the specimen size 'Big' than for other sizes. This is the expected behavior as the heterogeneity is

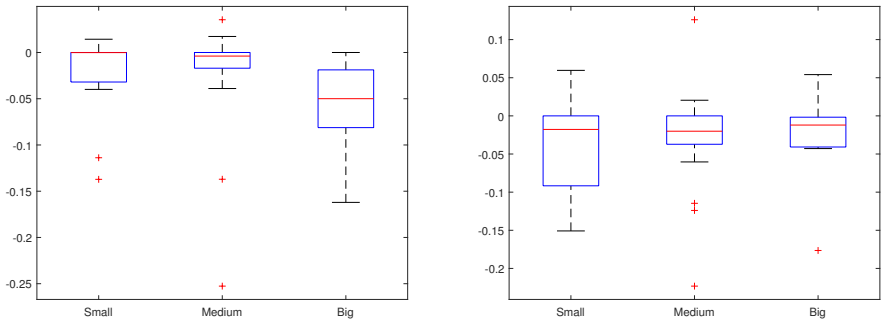

(a) ν_s

(b) ν_l

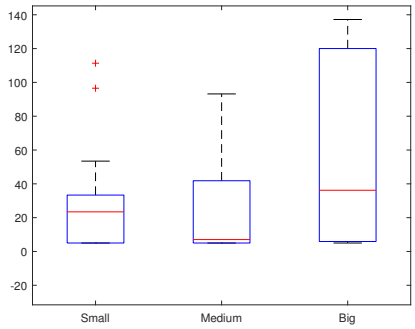

(c) τ_s (s)

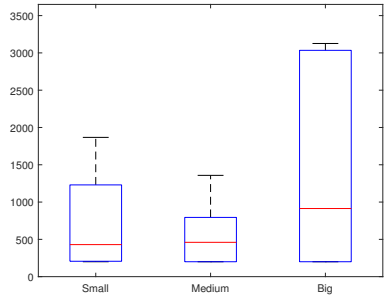

(d) τ_l (s) Outliers not plotted.

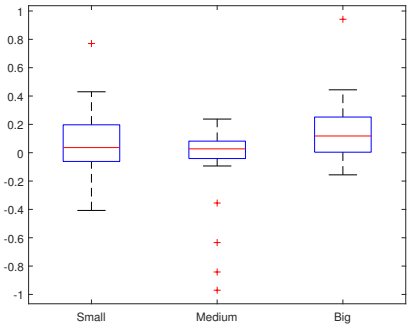

(e) ν_∞

Figure 49: Model parameters as a function of specimen size for the NW.

higher in a larger specimen and the mechanical behavior of each specimen is often controlled by its weaker points.

The random nature of the NW generates a high variation in the results. Tests performed on NW rectangular specimens of two different sizes with constant aspect ratio show and influence of the size on the elastic modulus, the strength, and the failure strain [Chen et al., 2016b] . The smaller specimen exhibits a gradually reduced

stress where the bigger specimen presents a fracture-like behavior. However, the strains used here (5%) are far from the fracture limits reported (40%).

The NW exhibits high strains in the direction perpendicular to the load [Martínez-Hergueta et al., 2015]. Compared to the LDPEO, the bands of high strain recorded in the NW are wider for one experiment (Fig. 32 and 33). This demonstrates the strong anisotropy of the NW. The strong strains at this position suggest more fibers are untangled allowing an easy displacement [Martínez-Hergueta et al., 2015]. More surprising is the appearance of a high strain gradient at 6.6 min (Fig. 32), which disappears at 9.9 min but is replaced by a strain gradient at another position (Fig. 32). This is attributed to fibers being slightly untangled in the upper band at 6.6 min leading to slippage as a deformation mechanism. This mechanism needs more energy to be activated so another untangled area of the specimen begins to deform [Martínez-Hergueta et al., 2015].

The increase of the NW specimen size and of the areal weight is responsible for a reduction of the gradual damage in the specimen. The deformation of the NW can included a destruction of the bonds, translating into damage of the material. The bond density decreases by 8% for 5 % engineering strain [Yazdani et al., 2019], a value that increases for thicker specimens. Since the specimen I tested were thicker, bond damage is expected during the stress relaxation test and is probably higher than 8%. When a bond is destroyed, the fibers can straighten, allowing a higher local strain. This mechanism originating from damage explains the presence of high strain bands and the large width of the bands compared to the LDPEO [Yazdani et al., 2019].

5.4.4 Conclusion

The influence of the size confirms that the LDPE is a homogeneous material while the LDPEO and the NW are both heterogeneous. Similarly, in previous studies, the thickness of microsphere-embedded PDMS specimens (125μm and 155μm) was found

a statistically significant factor influencing the VPR measured in stress relaxation [Dogru et al., 2018].

In asphalt mixtures, the VPR depends on aggregate ratios, confirming the influence of heterogeneity and anisotropy on the VPR of a material [Kassem et al., 2013]. However, this comparison should be nuanced as asphalts present a very different structure than polymers or NWs.

CHAPTER VI

INDUSTRIAL APPLICATION

6.1 Application

This chapter presents an application of the VPR computed in the previous chapter. The system considered is a web in a span between two rollers. The web is assume to be supported by enough rollers to neglect the effect of gravity. The web during the R2R process is under a constant stress σ at each extremity. The longitudinal axis is the x-axis, the transverse axis is the y-axis. The web considered is presented in figure 50. Out-of-plane effects are neglected.

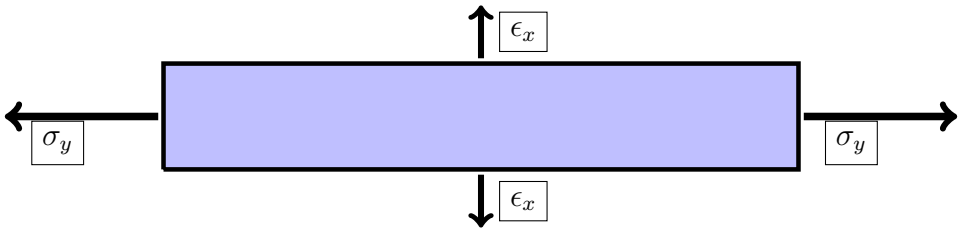

Figure 50: Web specimen considered

The web is under constant load, a stress controlled by the web tension. The lateral displacement of the web is computed from the equation 2.3.14, adapted from the computation of the VPR under creep condition. The absolute transverse strain is expected to increase with an increase of the stress applied, as predicted by linear viscoelasticity creep theory. The transverse strain is computed for different values of web stress (Table 11). The lateral displacement will then be studied for the various stress values and for multiple web widths. The width values are selected for each web

material as representative of an industrial process.

Table 11: Stress from web tension

Psi	500	600	700	800
MPa	3.44	4.13	4.82	5.51

The lateral displacement occurs rapidly as the load is applied. We assume the first print is calibrated and performed at that time and the registration errors happen afterwards, as the time-dependent effects arise. This represents a worst case scenario.

6.2 LDPE

The width values for the LDPE web are presented in table 12. The transverse strain for each web stress is computed for 20 min (Fig. 51). The negative value of the strain reflects the displacement of the web in the transverse direction, that is the Poisson effect.

Table 12: Width values of the LDPE web

Inches	30	40	50	60
Meters	0.76	1.01	1.27	1.52

The maximal strain obtained after 20 min for a pressure of 5.51 MPa is -0.003 or -0.3%. The lateral displacement is computed for different stress values (Fig. 52a) and width values (Fig. 52b).

For a stress of 5.51 MPa and a width of 1.52 m, the value of the lateral displacement at 1 s and at 20 min is 4.8324 mm and 4.668 mm, respectively.

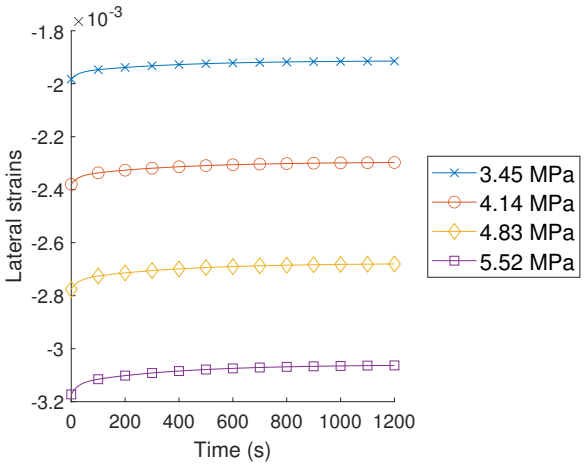

Figure 51: Transverse strain in a LDPE web according to web stress.

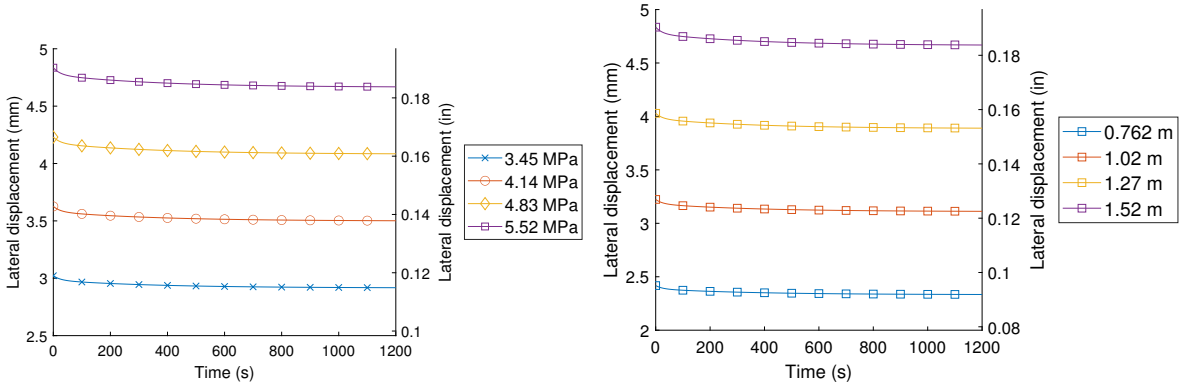

(a) Lateral displacement of the LDPE for a width of 1.52 m.

(b) Lateral displacement of the LDPE for a web stress of 5.51 MPa.

Figure 52: Lateral displacement of the LDPE web under various processing conditions.

6.3 LDPEO

The transverse strain and corresponding lateral displacement are computed for LDPEO webs of various widths (Table 13), using the VPR model for the LDPEO in MD.

Table 13: Width values of the LDPEO web.

Inches	150	200	250	300
Meters	3.81	5.08	6.35	7.62

The transverse strain is computed for the LDPEO web subject to various web stress values (Fig. 53).

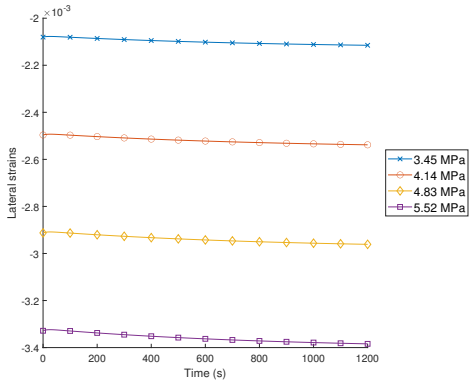

Figure 53: Transverse strain in a LDPEO web under web tension.

The maximal strain obtained after 20 min for a pressure of 5.51 MPa is -0.0034. The lateral displacement is computed for different stress values (Fig. 54a) and width values (Fig. 54b).

For a stress of 5.52 MPa and a width of 7.62 m, the maximal value of the lateral displacement at 1 s and 20 min is 25.36 mm and 25.79 mm, respectively. Although the

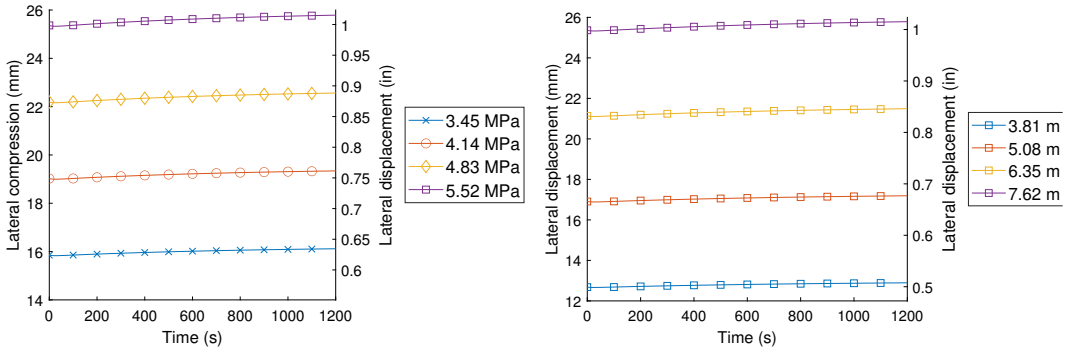

(a) Lateral displacement, LDPEO web, width 3.04 m.

(b) Lateral displacement, LDPEO web, stress 5.52 MPa.

Figure 54: Lateral displacement of the LDPEO web under various processing conditions.

values of lateral displacement are large, which is mostly due to the large dimensions of the rolls, their evolution with time is relatively limited.

6.4 NW

The transverse strain and corresponding lateral displacement are computed for NW webs of various widths (Table 14), using the VPR model for the NW in MD.

Table 14: Width values of the NW web

Inches	60	80	100	120
Meters	1.524	2.032	2.54	3.048

The transverse strain is computed for the NW web subject to various web stress values (Fig. 55).

The maximal strain obtained after 20 min for a pressure of 5.51 MPa is -0.0055. The lateral displacement is computed for different stress values (Fig. 56a) and width values (Fig. 56b).

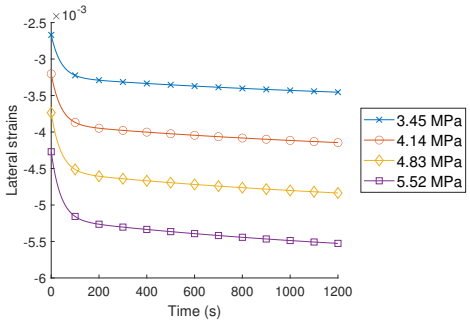

Figure 55: Transverse strain in a NW web under web tension.

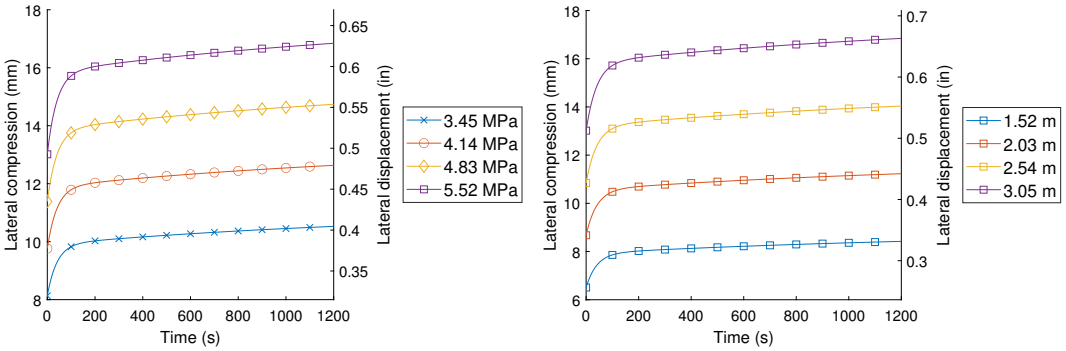

(a) Lateral displacement of the NW, width 1.524 m.

(b) Lateral displacement of the NW, stress 5.51 MPa.

Figure 56: Lateral displacement of the NW web under various processing conditions.

For a stress of 5.52 MPa and a width of 3.05 m, the maximal value of the lateral compression at 1 s and 20 min is 13.09 mm and 16.84 mm, respectively. The values of the lateral displacement for the NW evolve greatly with time, especially at short times, which could significantly impact the manufacturing process.

6.5 Comparison of the webs

In order to compare the behavior of the different webs, an imaginary case is considered where the web is subjected to a 5.51 MPa (800 Psi) stress.

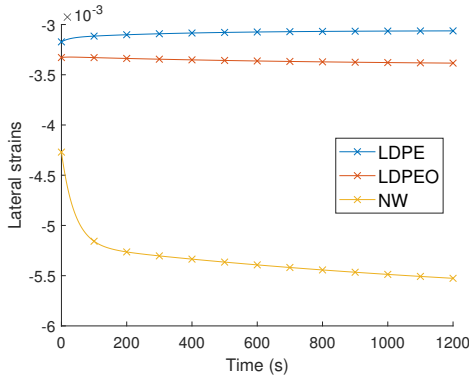

Figure 57: Transverse strain for the LDPE, LDPEO, and NW webs, at a stress of 5.51 MPa (800 Psi).

6.6 Error made considering the PR instead of the VPR

6.6.1 Error on the transverse strain

To estimate the importance of including the VPR, $\nu(t)$, compared to using the simpler elastic PR, ν_∞, the error in transverse strain is evaluated up to 1200 s and at 5.52 MPa for the LDPE (Fig. 58), the LDPEO (Fig. 59), and the NW (Fig. 60). The error on the strain is the relative error computed as

$$Error = \frac{|\varepsilon_{xx}(\nu(t)) - \varepsilon_{xx}(\nu_\infty)|}{|\varepsilon_{xx}(\nu(t))|} \tag{6.6.1}$$

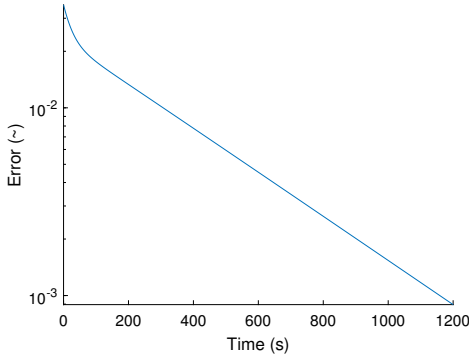

Figure 58: Error between the VPR and the PR strains, LDPE, stress 5.52 MPa (800 Psi).

The error on the transverse strain for the LDPE evolves from 0.035 at 1s to 8×10^{-4} after 20 min. The error values for LDPEO after 1 s and 1200 s are 0.023 and 0.006 for the MD and 0.033 and 0.008 for the CMD. The error values for the NW after 1s and 1200s are 0.35 and 0.051 for the MD and 0.5 and 0.079 for the CMD. For anisotropic materials, the error in CMD is slightly higher than the one in MD.

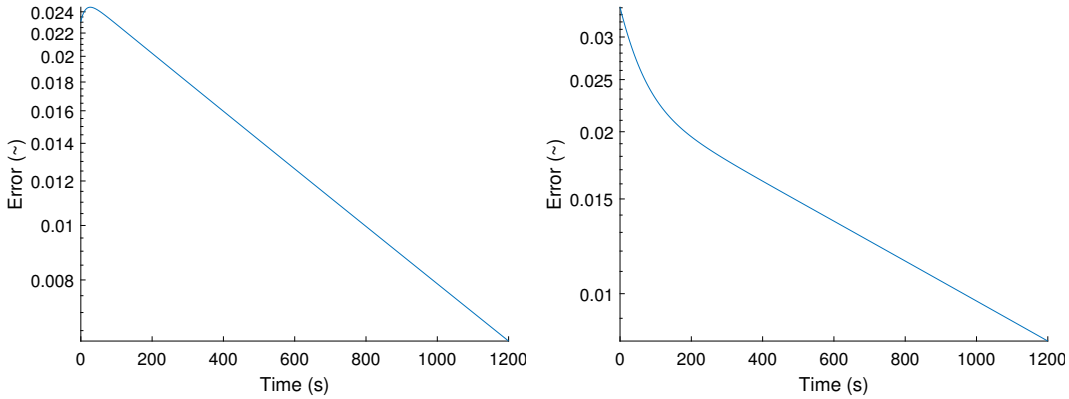

(a) MD (b) CMD

Figure 59: Error between the VPR and the PR strains, LDPEO, stress 5.52 MPa (800 Psi).

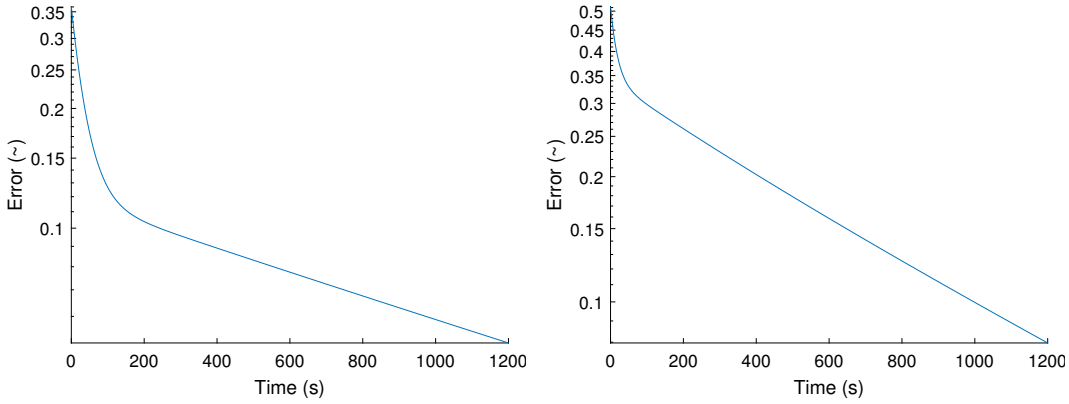

(a) MD (b) CMD

Figure 60: Error between the VPR and the PR strains, NW, stress 5.52 MPa (800 Psi).

6.6.2 Error on the lateral displacement

In this section, the width of the web will be included to compare the error for the lateral displacement obtained considering the PR and the VPR. The absolute error is evaluated for each web for a stress of 5.52 MPa (800 Psi)(Fig. 61). To allow a fair comparison between webs, the width is kept at 1 m (39.37 Inches).

The displacement error is computed as the absolute difference between the displacement obtained using the VPR and the displacement obtained using ν_∞.

$$Error = |Disp_{xx}(\nu_t) - Disp_{xx}(\nu_\infty)| \tag{6.6.2}$$

where $Disp$ is the displacement of the web.

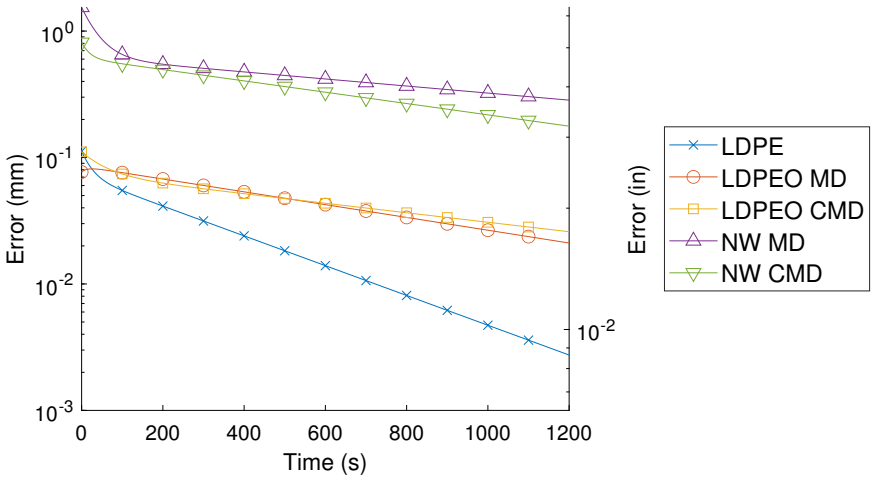

Figure 61: Absolute error on the lateral displacement obtained from the VPR and PR.

The error differs between materials but is mostly independent of direction for the anisotropic webs. The LDPE is the only web exhibiting an error reaching less than 10^{-3} mm after 1150 s ($\approx$ 19 min). However, the width of 1 m is not representative of industrial conditions in web handling. The following plot present the absolute error between the VPR and the PR for more realistic web widths (Fig. 62). The width used is 1.524 m (60 in) for the LDPE, 7.62 m (300 in) for the LDPEO MD, and 3.048 m (120 in) for the NW MD. The MD is the only relevant direction for industrial applications.

A registration error bigger than 0.01 mm (0.004 in) is perceptible to the human eye [Paukku & Parola, 2004] on a printed image. Consequently, a web exhibiting a lateral displacement of more than 0.01 mm would present registration errors. From this limit,

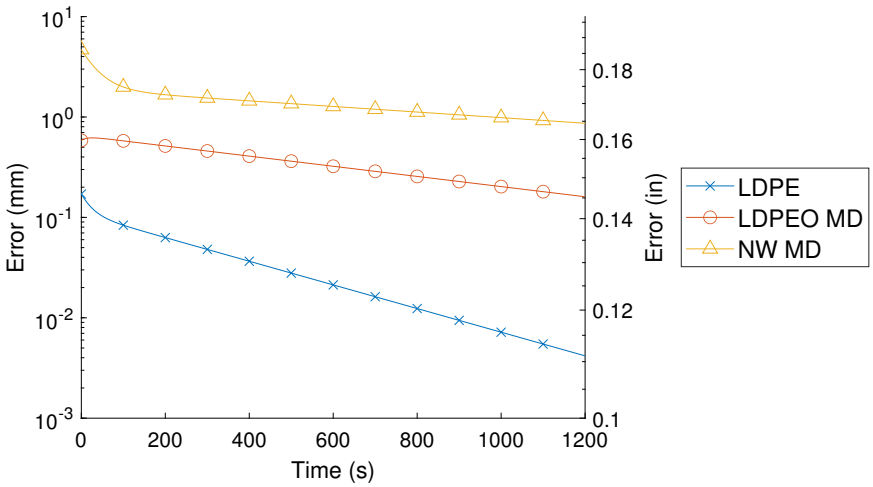

Figure 62: Absolute error on the lateral displacement obtained from the VPR and PR at different widths.

for a duration of less than 15 min, using the PR rather than the VPR to estimate the lateral displacement would lead to a registration error for any material. The LDPE is the only material for which the error reaches a value lower than 10^{-2} mm. This result shows the importance of using the VPR instead of the PR in registration models for industrial applications.

6.7 Conclusion

The transverse strain of the web is time-dependent as a result of the time-dependent properties of the material, characterized by the VPR. The error on the lateral displacement is far above the limit of the registration error.

These hypothetical scenarios also emphasize the importance of the web tension. Increasing the stress will reduce the time to reach the limit where the registration error is susceptible to occur.

Being able to characterize the VPR of the web material and hence predict the evolution of the lateral displacement through the R2R process can allow for a systematic control of the dynamics and avoid registration and alignment errors.

CHAPTER VII

CONCLUSION

The main objective of this thesis was to investigate the VPR and its usefulness to prevent registration errors during web handling. Creep and stress relaxation experiments combined with DIC were performed to measure the VPR of 3 different webs (LDPE, LDPEO, and NW) during 20 min for different sizes of dumbbell specimens oriented in MD and CMD. The VPR was computed with the analytical expression (2.3.4) for a stress relaxation test and (2.3.12) for a creep test. The influences of the material, the orientation, and the specimen size on the VPR are investigated by the means of multiple ANOVAs. Finally, the usefulness of the VPR to reduce registration errors is evaluated in hypothetical web handling cases of industrial relevance. The following list reviews the main findings from this work.

- The use of freely and readily available software such as NCORR has proven effective for 2D DIC on webs to quantify the longitudinal and transverse strains.

- Adapting the DIC experimental method to the different materials can be challenging. For example, the ink does not hold on each material the same way and the experimental parameters like maximal stress or strain have to be adapted to stay in the linear region. Because some materials are heterogeneous, a large number of repetitions have to be performed to ensure a statistical correlation in the results.

- Creep measurements present additional difficulties compared to stress relax-

ation. Creep measurements did not provide reliable quantification.

- The short time measurements during the first few seconds did not correlate well with the DIC method because the data is noisy.

- In general, the material influences the time-dependent components of the VPR. This influence of the material is attributed to the different deformation mechanisms in action, which depend on the material structure.

- The influence of the specimen size on the VPR seems to reflect the heterogeneity of the web. As the LDPE is a homogeneous material, specimen size has no influence on the VPR. For the heterogeneous LDPEO and the NW, the specimen size significantly influences the long relaxation time.

- In heterogeneous materials, the strain field also presents strong heterogeneities, namely high strains bands. These localized high gradients were only recorded for LDPEO and NW specimens.

- The lateral displacement computed from the VPR differs from the one computed from the elastic PR. This difference is above the limit creating a registration error visible with the naked eye.

The following conclusions can be stated from this work.

- The non-homogeneous deformations in heterogeneous materials can significantly increase the registration error if they occur at a printing location.

- The prediction of the lateral position of the web computed from a simple quasi-static time-dependent model significantly varies when considering the PR or the VPR. This preliminary assessment indicates dynamic registration models could benefit from including a time-dependent Poisson's ratio.

CHAPTER VIII

FUTURE WORK

This work can be expanded is multiple interesting directions, experimental and theoretical.

8.1 Short-time VPR measurements

Measuring the VPR at short times has proven difficult in this study and in others reported in the literature. Developing a method independent of the machine regulating through a loading ramp would be greatly beneficial to this specific measurement. As is often the case in viscoelasticity, to eliminate undue influences at short times, the use of frequency loading in Dynamic Mechanical Analysis (DMA) is preferred to access steady-state behavior. One could envision a measurement of longitudinal and transverse strains with DIC during DMA tests at different frequencies.

Building such an experimental setup presents multiple challenges. First, the camera needs to be correlated with the DMA measurements of stress and strain through time and the current software controlling the machine does not allow for such a calibration. Second, the number of images taken by the camera needs to be high enough to perform a relevant DIC through a strain cycle. Finally, the strain cycle needs to be of high enough amplitude to allow for strain measurement through DIC and small enough to remain in the small strain vibration region necessary for proper DMA measurements. This implies a very fine patterning of small specimens and the use of a high resolution camera. Nonetheless, these practical experimental difficulties are all

workable.

This experiment would lead to a set of data integrating the influence of time on the Poisson's ratio. A procedure would then have to be developed to extract the actual VPR from this data set. Indeed, in addition to the complex modulus traditionally measured in DMA, a complex Poisson's ratio would be quantified. However, there is no guarantee that the longitudinal strain and the transverse strain would be perfectly in phase. Consequently, the complex PR must include the possibility of a phase shift between the orthogonal strains, which would lead to some complexity in the data processing.

8.2 VPR model

In this study, the VPR has been crudely fitted with a two-term Prony series following traditional forms for the time-dependent material functions, relaxation modulus and creep compliance. This choice has however not been validated or justified theoretically. Although sum of exponential functions are widely used for their practicality, there is no guarantee that this would best represent the VPR time evolution. More importantly, the number of terms in the series can have an influence on the goodness of fit and on the relaxation times identified. It would be interesting to assess how many relaxation times are necessary to correctly represent the relaxation modulus and the creep compliance for each material and compare it to the function best representing the VPR. As each relaxation time is supposed to stand for a specific relaxation mechanism, these should correlate between the different functions.

8.3 Linking the VPR to the origin of the viscoelasticity

A few comments have been made in this study on the the link between VPR variations and deformation mechanisms. We chose materials with industrial relevance independently of their structure and formulation. As a consequence, these materials

vary widely in structure, which we have not studied in details. A full micromechanical study of the origin of the time-dependence of the VPR would particularly benefit any predictive effort of that material property and any approach dedicated to manipulating it. For example, numerous research efforts have recently been focused on producing auxetic materials through ever smaller structural tuning. A full understanding of microscopic mechanisms underlying the VPR, which is basically the evolution with time of the material ability to deform rather than change volume, would open possibilities of designing materials for specific VPR functions.

8.4 Heterogeneity, anisotropy, and VPR

The VPR literature is often limited to homogeneous isotropic materials. However, those are not relevant manufacturing materials since most webs are intrinsically anisotropic due to their manufacturing process and/or heterogeneous due to their composition. Because two of the webs studied here were heterogeneous anisotropic, we have measured numerous "anomalies" in the behavior. Local strain heterogeneities (high strain bands) in anisotropic materials were particularly intriguing as they seem to appear in specific directions but at locations that evolve with time. The degree of heterogeneity of the material is thought to have an impact on these bands, although the question has not been further explored in this study because of insufficient time. These bands also indicate that the VPR, along with other material properties, is locally varying in heterogeneous materials.

Comparing the local VPR distribution according to heterogeneity and in correlation with detailed structure measurements would inform better models. It would also prevent potential irregularities and errors in a printing process, for example by determining a maximum acceptable degree of heterogeneity for a specific process to avoid chronic registration errors.

REFERENCES

[Alanazi et al., 2019] Alanazi, N., Kassem, E., Grasley, Z., & Bayomy, F. (2019). Evaluation of viscoelastic Poisson's ratio of asphalt mixtures. *International Journal of Pavement Engineering*, 20(10), 1231–1238.

[Balani et al., 2014] Balani, K., Verma, V., Agarwal, A., & Narayan, R. (2014). *Physical, Thermal, and Mechanical Properties of Polymers*. Hoboken, NJ, USA: John Wiley & Sons, Inc.

[Bauer & Farris, 1989] Bauer, C. L. & Farris, R. J. (1989). Determination of poisson's ratio for polyimide films. *Polymer Engineering and Science*, 29(16), 1107–1110.

[Blaber & Antoniou, 2017] Blaber, J. & Antoniou, A. (2017). Ncorr - Instruction Manual.

[Chen et al., 2016a] Chen, N., Koker, M. K., Uzun, S., & Silberstein, M. N. (2016a). In-situ X-ray study of the deformation mechanisms of non-woven polypropylene. *International Journal of Solids and Structures*, 97-98, 200–208.

[Chen et al., 2016b] Chen, N., Koker, M. K., Uzun, S., & Silberstein, M. N. (2016b). In-situ X-ray study of the deformation mechanisms of non-woven polypropylene (Supplementary material). *International Journal of Solids and Structures*, 97_98(607), 200–208.

[Delin et al., 1995] Delin, M., Rychwalski, R. W., Kubat, M. J., & Kubat, J. (1995). Volume changes during stress relaxation in polyethylene. *Rheologica Acta*, 34(2), 182–195.

[Deng et al., 2015] Deng, Y., Yi, P., Peng, L., Lai, X., & Lin, Z. (2015). Flow behavior of polymers during the roll-to-roll hot embossing process. *Journal of Micromechanics and Microengineering*, 25(6), 065004.

[Dobnik Dubrovski et al., 2019] Dobnik Dubrovski, P., Novak, N., Borovinšek, M., Vesenjak, M., & Ren, Z. (2019). In-Plane Behavior of Auxetic Non-Woven Fabric Based on Rotating Square Unit Geometry under Tensile Load. *Polymers*, 11(6), 1040.

[Dogru et al., 2018] Dogru, S., Aksoy, B., Bayraktar, H., & Alaca, B. E. (2018). Poisson's ratio of PDMS thin films. *Polymer Testing*, 69, 375–384.

[Dogumak, 2020] Dogumak (2020). 10/07/2020. https://www.dogumak.com/products/roll-splitter/.

[Dwivedula et al., 2006] Dwivedula, R. V., Zhu, Y., & Pagilla, P. R. (2006). Characteristics of active and passive dancers: A comparative study. *Control Engineering Practice*, 14(4), 409–423.

[Farfán-Cabrera et al., 2017] Farfán-Cabrera, L. I., Pascual-Francisco, J. B., Barragán-Pérez, O., Gallardo-Hernández, E. A., & Susarrey-Huerta, O. (2017). Determination of creep compliance, recovery and Poisson's ratio of elastomers by means of digital image correlation (DIC). *Polymer Testing*, 59, 245–252.

[Giovagnoni, 1994] Giovagnoni, M. (1994). On the direct measurement of the dynamic Poisson's ratio. *Mechanics of Materials*, 17(1), 33–46.

[Good et al., 1997] Good, J. K., Kedl, D. M., & Shelton, J. J. (1997). Shear wrinkling in isolated spans. In *TAPPI* (pp. 462–480). Stillwater, OK: Oklahoma State University.

[Hirsekorn et al., 2018] Hirsekorn, M., Marcin, L., & Godon, T. (2018). Multi-scale modeling of the viscoelastic behavior of 3D woven composites. *Composites Part A: Applied Science and Manufacturing*, 112(July), 539–548.

[Instron, 2013] Instron (2013). Setting proportional gain for load control. 11/09/2018. http://www.instron.us/.

[Kamide & Saito, 1985] Kamide, K. & Saito, M. (1985). Thermal Analysis of Cellulose Acetate Solids with Total Degrees of Substitution of 0.49, 1.75, 2.46, and 2.92. *Polymer Journal*, 17(8), 919–928.

[Kassem et al., 2013] Kassem, E., Grasley, Z. C., & Masad, E. (2013). Viscoelastic Poisson's Ratio of Asphalt Mixtures. *International Journal of Geomechanics*, 13(2), 162–169.

[Kimoto et al., 1990] Kimoto, M., Nagata, I., Minowa, A., Moriwaki, K., & Watanabe, T. (1990). Evaluation of disbondings and measurement of Poisson's ratio for plastic composites using holographic interferometry. *Journal of Applied Polymer Science*, 40(78), 1085–1093.

[Kreyszig, 2012] Kreyszig, E. (2012). *Advanced engineering*. Number 181. New York, NY: New York : Wiley, 1993 edition.

[Kugler et al., 1990] Kugler, H. P., Stacer, R. G., & Steimle, C. (1990). Direct Measurement of Poisson's Ratio in Elastomers. *Rubber Chemistry and Technology*, 63(4), 473–487.

[Lee et al., 2020] Lee, J., Byeon, J., & Lee, C. (2020). Theories and Control Technologies for Web Handling in the Roll-to-Roll Manufacturing Process. *International Journal of Precision Engineering and Manufacturing-Green Technology*, 7(2), 525–544.

[Li et al., 2020] Li, C., Xu, H., & Chen, S.-C. (2020). Design of a precision multi-layer roll-to-roll printing system. *Precision Engineering*, 66, 564–576.

[Lu et al., 1997] Lu, H., Zhang, X., & Knauss, W. G. (1997). Uniaxial, shear, and poisson relaxation and their conversion to bulk relaxation: Studies on poly(methyl methacrylate). *Polymer Engineering & Science*, 37(6), 1053–1064.

[Martínez-Hergueta et al., 2015] Martínez-Hergueta, F., Ridruejo, A., González, C., & LLorca, J. (2015). Deformation and energy dissipation mechanisms of needle-punched nonwoven fabrics: A multiscale experimental analysis. *International Journal of Solids and Structures*, 64-65, 120–131.

[Mehrez et al., 2015] Mehrez, L., Kassem, E., Masad, E., & Little, D. (2015). Stochastic Identification of Linear-Viscoelastic Models of Aged and Unaged Asphalt Mixtures. *Journal of Materials in Civil Engineering*, 27(4), 04014149.

[Negahban et al., 2007] Negahban, M., Strabala, K., Delabarre, P., Goel, A., Feng, R., & Grene, J. (2007). Temperature Dependence of the Back-Stress in Shear for Glassy Polycarbonate. *Macromolecular Symposia*, 258(1), 142–151.

[Noh et al., 2010] Noh, J., Yeom, D., Lim, C., Cha, H., Han, J., Kim, J., Park, Y., Subramanian, V., & Cho, G. (2010). Scalability of Roll-to-Roll Gravure-Printed Electrodes on Plastic Foils. *IEEE Transactions on Electronics Packaging Manufacturing*, 33(4), 275–283.

[O'Brien et al., 2007] O'Brien, D. J., Sottos, N. R., & White, S. R. (2007). Cure-dependent Viscoelastic Poisson's Ratio of Epoxy. *Experimental Mechanics*, 47(2), 237–249.

[Pan et al., 2020] Pan, S., Azoug, A., & Good, J. K. (2020). Viscoelastic web curl due to storage in wound rolls. *TAPPI*.

[Park et al., 2018] Park, J., Kim, D., & Lee, C. (2018). Contact angle control of sessile drops on a tensioned web. *Applied Surface Science*, 437, 329–335.

[Paukku & Parola, 2004] Paukku, J. & Parola, M. (2004). Measurement method and analysis of dynamic dimensional stability of paper web. In *Proceedings of the Technical Association of the Graphic Arts, TAGA* (pp. 561–577).

[Poisson, 1829] Poisson, S. (1829). *Mémoires de l'Académie des sciences de l'Institut de France*, volume 8. Paris: Firmin-Didot (Paris), Gauthier-Villars (Paris), 1829 edition.

[Roisum, 1995] Roisum, D. (1995). The 10 commandments of web machine design. In *TAPPI* (pp. 416–425). Stillwater, OK.

[Seshadri & Pagilla, 2013] Seshadri, A. & Pagilla, P. R. (2013). Comparison of control strategies for roll-to-roll printing presses. In *TAPPI* (pp. 375 – 392). Stillwater, OK: Oklahoma State University.

[Seshadri et al., 2013] Seshadri, A., Pagilla, P. R., & Lynch, J. E. (2013). Modeling Print Registration in Roll-to-Roll Printing Presses. *Journal of Dynamic Systems, Measurement, and Control*, 135(3), 1–11.

[Shi, 2019] Shi, J. (2019). *The Interaction Between Webs and Rollers in Roll-To-Roll Manufacturing Process Machines*. Thesis, Oklahoma State University.

[Sperling, 2005] Sperling, L. (2005). *Introduction to Physical Polymer Science*. Wiley, 4^{th} edition.

[Theocaris, 1964] Theocaris, P. (1964). Creep and relaxation contraction ratio of linear viscoelastic materials. *Journal of the Mechanics and Physics of Solids*, 12(3), 125–138.

[Tscharnuter et al., 2011a] Tscharnuter, D., Jerabek, M., Major, Z., & Lang, R. W. (2011a). On the determination of the relaxation modulus of PP compounds from arbitrary strain histories. *Mechanics of Time-Dependent Materials*, 15(1), 1–14.

[Tscharnuter et al., 2011b] Tscharnuter, D., Jerabek, M., Major, Z., & Lang, R. W. (2011b). Time-dependent poisson's ratio of polypropylene compounds for various strain histories. *Mechanics of Time-Dependent Materials*, 15(1), 15–28.

[Tschoegl, 1989] Tschoegl, N. W. (1989). *The Phenomenological Theory of Linear Viscoelastic Behavior An Introduction*. Berlin: Springer Berlin Heidelberg, 1989 edition.

[Tschoegl et al., 2002] Tschoegl, N. W., Knauss, W. G., & Emri, I. (2002). Poisson's ratio in linear viscoelasticity - a critical review. *Mechanics Time-Dependent Materials*, 6(1), 3–51.

[Tsou et al., 1995] Tsou, A., Greener, J., & Smith, G. (1995). Stress relaxation of polymer films in bending. *Polymer*, 36(5), 949–954.

[Wang et al., 2016] Wang, J., Xu, Y., Zhang, W., & Moumni, Z. (2016). A damage-based elastic-viscoplastic constitutive model for amorphous glassy polycarbonate polymers. *Materials & Design*, 97, 519–531.

[Yazdani et al., 2019] Yazdani, H., Ghasemi, H., Wallace, C., & Hatami, K. (2019). Mechanical properties of carbon nanotube-filled polyethylene composites: A molecular dynamics simulation study. *Polymer Composites*, 40(S2), E1850–E1861.

[Yee & Takemori, 1982] Yee, A. F. & Takemori, M. T. (1982). Dynamic bulk and shear relaxation in glassy polymers. I. Experimental techniques and results on PMMA. *Journal of Polymer Science: Polymer Physics Edition*, 20(2), 205–224.

[Zhang et al., 2004] Zhang, X. M., Elkoun, S., Ajji, A., & Huneault, M. A. (2004). Oriented structure and anisotropy properties of polymer blown films: HDPE, LLDPE and LDPE. *Polymer*, 45(1), 217–229.

APPENDIX

```
temp = intersect(find(~data_dic_save.strains(5).plot_exx_ref_formatted),
    ...
    find(~data_dic_save.strains(5).plot_eyy_ref_formatted)); % Find out-
       of-ROI pixels
Mask = zeros(size(data_dic_save.strains(1).plot_exx_ref_formatted)) + 1;
Mask(temp) = 0; % Set out-of-ROI pixels to 0
% Get the data
ROI = Mask(any(Mask,2),:);  % Remove rows with only zeros wrt the ROI
ROI = ROI(:,any(Mask,1));  % Remove columns with only zeros wrt the ROI
% Initialize the vectors
s1 = zeros(size(Mask,1),size(Mask,2));
s2 = zeros(size(Mask,1),size(Mask,2));
n = 1; % Define the index of the frame considered
% For the x direction
Mask = data_dic_save.strains(1).roi_ref_formatted.mask; % Get the ROI
s1 = data_dic_save.strains(n).plot_exx_ref_formatted; % Strain on the
   transversal axis ...
 % of the specimen computed by Ncorr
s1 = s1(any(Mask,2),:);  % Remove rows with only zeros wrt the ROI
s1 = s1(:,any(Mask,1));  % Remove columns with only zeros wrt the ROI
s1 = fliplr(s1);         % Inverse the picture
s1_median = median(s1,'all');   % Strain recorded along x
% For the y direction
s2 = data_dic_save.strains(n).plot_eyy_ref_formatted; % Strain on the
   axial axis ...
 % of the specimen computed by Ncorr
s2 = s2(any(Mask,2),:);  % Remove rows with only zeros wrt the ROI
s2 = s2(:,any(Mask,1));  % Remove columns with only zeros wrt the ROI
s2 = fliplr(s2);         % Inverse the picture
s2_median = median(s2,'all');      % Strain recorded along y
```

Figure 63: Code used to extract the strains from the Ncorr results.

```
%% Compute the Poisson's ratio and save it in the structure
ParforLoopPR(Specimen_List)
%%
function a = ParforLoopPR(Specimen_List)
% Generate the progress bar
D = parallel.pool.DataQueue;
f = waitbar(0, 'Compute the Poisson''s ratio', 'CreateCancelBtn', @(src,
    event) setappdata(gcbf(), 'Cancelled', true));
setappdata(f, 'Cancelled', false);
afterEach(D, @nUpdateWaitbar);
N = size(Specimen_List,2); % Total number of itteration to do (number of
    specimen in the pool)
p = 1; % Number of specimen performed done;

% Compute the Poisson's ratio
parfor i =1:size(Specimen_List,2)
    if ~isempty(Specimen_List(i).SpecimenName) % Removed incorrect
       entree if present
        Strain_extract(Specimen_List(i).SpecimenFolder, 1); % Function
           to extract the strains. ...
        % 1 is the index of the specimen processed
    end
    send(D, i); % Update the progress bar
end
    function nUpdateWaitbar(~)
        waitbar(p/N, f, ['Poisson''s ratio ', num2str(p), ' over ',
           num2str(N), ' done.']);
        p = p + 1;
        % Check to see if the cancel button was pressed.
        if getappdata(f, 'Cancelled')
            fprintf('Simulation cancelled.\n');
            error('Simulation cancelled');
        end
    end

close(f)
end
```

Figure 64: Code used to process several specimen at the same time.

```
i = 1; % Index of the specimen
X = Specimen_List(i).Instron.time; % [s]
Y = Specimen_List(i).Instron.strain;
[X, Y] = prepareCurveData(X, Y); % Check if the vactors have the same
    size, remove Nan values.

epsilon_0 = mean(Y(round(0.3*end):end)); % Value constant
% Compute the Poisson's ratio
T = Specimen_List(i).Time; % [s]
X_median = Specimen_List(i).Strain.median.True.exx;  % Load the strains
[T, X_median] = prepareCurveData(T, X_median);
mu_median = - X_median ./ epsilon_0; % VPR
```

Figure 65: Code used to compute the VPR for a stress relaxation test.

```
T = Specimen_List(i).Instron.time;   % [s]
Y = Specimen_List(i).Instron.strain; %  [m]
Z = Specimen_List(i).Instron.stress*1e6;  % [Pa]
[T, Y, Z] = prepareCurveData(T, Y, Z); % Check if the vactors have the
    same size, remove Nan values.

sigma_0 = mean(Z(round(0.3*end):end));  %  Value constant [Pa]
D_g =1e-8; % Defined the creep complicance
d = Y ./ sigma_0; % Creep compliance [1/Pa]

X_median = Specimen_List(i).Strain.median.True.exx;   % Load the strains
Y_median = Specimen_List(i).Strain.median.True.eyy;   % Load the strains
[d, X_median, Y_median] = prepareCurveData(d, X_median, Y_median);  %
    Check if the vactors have ...
   % the same size, remove Nan values.

mu_creep_median = -X_median ./ Y_median; % Instantaneous Poisson ratio
    for a creep test

mu_median = (1/D_g) .* mu_creep_median .* d; % VPR for a creep test
```

Figure 66: Code used to compute the VPR for a creep test.

```
X = time; % Time values
Y = VPR; % VPR values
[Xdata, Ydata] = prepareCurveData(X,Y)

X_min = 2; % Index of the begining of the curve to fit
X_max = size(X,1);  % Index of the end of the curve fited

tau_min = 5; % Minimal value for tau
tau_max = 200; % Value between long and short terms
C_tol = 0.15; % Tolerence used for the constant
K = 100 ; % Abs value of the coeficient (x(1) and x(2)) used for the
    upper and lower limit

% F = @(x,t)x(1)*exp(-t/x(2)) + x(3)*exp(-t/x(4))+x(5); % Define the
    model use
F = @(x,t) diff(x(1))-x(2)*t;


[Xdata, Ydata] = prepareCurveData(X(round(X_min): round(X_max)), Y(round
    (X_min): round(X_max))); % ...
      %   Data to fit, remove the values outside X_min:X_max
C_est = mean(Ydata(round(0.8*end):end)); % Estimated value of the end of
     the curve. Is the constant is the model.
x0 = rand(1,5); % Define the start points as random points

% Define the lower limit of the coefficient
lb = [-K tau_min -K tau_max min([(1-C_tol)*C_est, (1+C_tol)*C_est])];
% Define the upper limit of the coefficient
up = [0 tau_max 0 +Inf      max([(1-C_tol)*C_est, (1+C_tol)*C_est])];
% Performe the fit. x1 contains the coeficients, resnorm is the squared
% norm of the residual.
[x,resnorm,exitflag,output] = Fit_curves(F,Xdata,Ydata, lb, up, x0);

function [x,resnorm,exitflag,output] = Fit_curves(F,X,Y, lb, up, x0)
options = optimoptions('lsqcurvefit'); % Fit the function with
    lsqcurvefit
% Define the treshold options
options.MaxIterations = 15e5;
options.MaxFunctionEvaluations = 15e5;
options.OptimalityTolerance = 1e-10;
options.StepTolerance = 1e-10;
options.FunctionTolerance = 1e-10;
options.UseParallel = true; % increase the performnce
options.FiniteDifferenceType = 'central'; % Slower but a little more
    precise
[x,resnorm,~,exitflag,output] = lsqcurvefit(F,x0,X,Y, lb, up, options);
end
```

Figure 67: Code used to fit the data.

VITA

Clement Brousse

Candidate for the Degree of

Master of Science

Thesis: THE VISCOELASTIC POISSON'S RATIO OF WEBS

Major Field: Mechanical engineering

Biographical:

Education: Mechanical Engineering

Completed the requirements for the Master of Science (M.Sc) in Mechanical Engineering at Oklahoma State University, Stillwater, Oklahoma in December 2020.

Completed the requirements for the Master of Engineering (M.Eng.) in Mechanical Engineering at Ecole Catholique des Arts et Métiers, 67300 Schiltigheim, France in 2017.

Completed the requirements for the Bachelor of Science (B.Sc.) in Mechanical Engineering at Ecole Catholique des Arts et Métiers, 67300 Schiltigheim, France in 2017.